ADJUSTABLE SPEED DRIVE BEARING FAULT DETECTION VIA SUPPORT VECTOR MACHINE INCORPORATING FEATURE SELECTION USING GENETIC ALGORITHM

A Dissertation presented to

The Faculty of the Graduate School

at the University of Missouri-Columbia

In Partial Fulfillment

of the Requirements for the Degree

Doctor of Philosophy

By

KAPTAN TEOTRAKOOL

Dr. Michael J. Devaney, Dissertation Supervisor

DECEMBER 2007

The undersigned, appointed by the dean of the Graduate School, have examined the dissertation entitled

ADJUSTABLE SPEED DRIVE BEARING FAULT DETECTION

VIA SUPPORT VECTOR MACHINE INCORPORATING FEATURE SELECTION

USING GENETIC ALGORITHM

presented by Kaptan Teotrakool,

a candidate for the degree of doctor of philosophy,

and hereby certify that, in their opinion, it is worthy of acceptance.

Professor Michael Devaney

Professor Dominic Ho

Professor Robert O'Connell

Professor Marjorie Skubic

Professor Chi-Ren Shyu

To my mother

Udon Teotrakool

who has emphasized the importance of education and guided me throughout my life.

To my father

Roongthip Teotrakool

who has been my role-model for hard work, persistence, and personal sacrifices

and who instilled his contemplativeness and wisdom into me.

To my wife and soul mate

Arunee May Teotrakool

who has been proud and tirelessly supportive of my work

and who always wants me to be a better person in everyway.

To my son

Akira Keene Teotrakool

who reenergizes me every moment with his smiles and laughs

and who helped me realize my true potential.

ACKNOWLEDGEMENTS

My thanks and deepest appreciation to my advisor, Dr. Michael J. Devaney, for his wisdom, guidance, encouragement, and countless support throughout the doctoral program. He demonstrated his pure efforts as an educator and set the best examples of professional dedication as an engineer.

I would like to express my gratitude to the members of my doctoral committee for their assistance and guidance. I am very grateful for the advice, guidance, and generosity I received from Dr. Robert O'Connell and Dr. Marjorie Skubic. I deeply appreciate Dr. Dominic K. C. Ho for his wisdom, guidance, and advice. I owe a special note of gratitude to Dr. Chi-Ren Shyu for ever available helps.

I extend many thanks to my colleagues and friends, especially Dr. Levent Eren, who inspired my research and of whom suggestions and comments were very insightful and valuable, and Jaturon Harnsomburana, who helped me expedite my data processing considerably. I would like to also thank Nicholas J. Hudson who constantly gave constructively uncompromising comments on my work.

Lastly, I would like to thank the Royal Thai Navy for having given me the greatest opportunity in my life to study in the U.S.A. since my baccalaureate. The dissertation would never have been written without their initial support.

TABLE OF CONTENTS

LIST OF FIGURES

LIST OF TABLES

ADJUSTABLE SPEED DRIVE BEARING FAULT DETECTION VIA SUPPORT VECTOR MACHINE INCORPORATING FEATURE SELECTION USING GENETIC ALGORITHM

Kaptan Teotrakool

Dr. Michael J. Devaney, Dissertation Supervisor

ABSTRACT

Adjustable Speed Drives (ASD's) are increasingly used for process control and energy conservation in many commercial and industrial applications. Like other electrical rotating machines, a major cause of ASD failures is bearing failures. Though bearings are very inexpensive to replace, their problems are among the most difficult to detect. This dissertation presents a novel method to detect bearing defects in ASD's.

Motor current signature analysis (MCSA) is a non-intrusive machine condition monitoring method. It analyzes changes in the motor stator currents using frequency spectral analysis. The method relies on wavelet packet decomposition due to the non-stationary nature of ASD loads, which affect both current and speed.

Most modern ASD systems accomplish their variable speed by utilizing pulse-width-modulation (PWM) inverters to vary the fundamental frequency of the input voltage waveforms to their motors. Since the input voltage is PWM, it contains a significant number of harmonic components. When these harmonics are modulated by

the mechanical bearing frequencies, more harmonics are introduced. As a result of this modulation, a substantial number of additional frequencies are introduced into the current waveform. In addition, the ASD elevates the level of EMI noise and further complicates the detection of the defective bearing frequency components. Thus, detecting bearing problems by simply comparing the rms values of the wavelet packet coefficients of those frequencies is not feasible.

The proposed method combines MCSA, wavelet packet decomposition, a genetic algorithm, and a support vector machine to accomplish bearing fault detection in adjustable speed drives. The Support Vector Machine (SVM) in conjunction with the Genetic Algorithm (GA) is applied to the rms values of the wavelet packet coefficients to obtain optimal classifiers for classifying both healthy and defective bearings in ASD systems. The SVM is a method to find an optimal classifier for both linearly separable and linearly non-separable data. For linearly non-separable data, the SVM maps the data into higher dimensions before finding a classifier. With the SVM, a classifier for high-dimensional wavelet packet current data can be obtained. The GA works to select significant frequency bands and eliminates those less relevant. The SVM, using selected frequency bands from the wavelet packet decomposition, can find a classifier that can separate healthy and defective bearings more effectively.

CHAPTER 1 INTRODUCTION

1.1 Relevance

Adjustable Speed Drives (ASD's) are increasingly used for process control and energy conservation in many commercial and industrial applications. Since industry relies heavily on continuous operation of ASD systems, failures of these machines are critical and often lead to financial losses resulting from disruption of production, machine replacement, and human injury and/or fatality. A basic ASD system, consisting of a drive and a motor, costs more than twice as much as the motor alone. Bearing faults are the biggest cause of ASD failures, though the costs of the bearings are much lower than that of either the motor or the drive and certainly less than the additional expenses/liabilities associated with a catastrophic machine failure. To avoid losses and protect investment, predictive maintenance on ASD bearings is highly recommended for early detection and schedulable replacement of defective bearing when the ASD can be removed from service. Thus, significant research effort has focused on the detection of bearing faults in ASD's.

Most ASD failures are caused by bearing faults. Studies indicate that bearing problems contribute to over 40% of all motor failures [1]. Unlike line-driven motors, which run at a relatively constant speed, ASD applications, such as those in heating, ventilation and air conditioning (HVAC) systems, maintenance of negative pressure in nuclear power plants, and production lines in manufacturing plants, require ASD's to operate at variable speeds. The bearings are continuously strained as ASD motors are

accelerated and decelerated during their operations. This variation significantly increases stress on the bearings in comparison to those of line-driven motors [2]. In addition to the mechanical stresses, damage from electrical discharge machining (EDM) resulting from high dv/dt of the ASD contribute to accelerated bearing ware and bearing failures. EDM results from transient currents flowing from the motor windings to ground through the bearings via an imbalance in the stator stray capacitances. EDM creates microscopic pits on the inner and outer races of the bearings of ASD machines [3, 4]. The *dv/dt* current flowing through the capacitances induces a change in the chemical composition in the lubricant, and ultimately causes bearing lubricant breakdown [3]. Due to both the added mechanical stresses and EDM, ASD systems are more likely to experience greater frequency of bearing failures.

For the early detection of bearing defects, the health of bearings can be observed by several analytical methods. Vibrational, thermal, and acoustic analyses require the placement of sensors or transducers on the machines. Some large motors may already have these sensors built-in. However, this is not likely the case for smaller motors since it is economically impractical. To check small and medium-sized machines, the system may have to be shut down so that machines can be safely accessible and to enable the attachment of diagnostic transducers to the motors. In some critical cases, such as the negative pressure maintenance system in a nuclear power plants, periodical monitoring during the operation may be infeasible. Moreover, all these analysis techniques require a great amount of expert man-power, resulting in considerable expense. Hence, it is virtually impossible to continuously monitor the health of the bearings of ASD's with such techniques.

As an alternative method, Motor Current Signature Analysis (MCSA) is a non-intrusive technique used to determine the health of a machine by analyzing the spectral components of its stator current [1]. In traditional MCSA, the steady state stator current of the motor is decomposed into frequency spectrum components using the Fourier Transform (FT). Then, the magnitudes of the characteristic frequency bands of the signal are compared to baseline values to detect any changes that may be indicative of failures in the motor bearings.

The ASD motor is fed by the pulse-width modulation (PWM) inverter with sharp-edged voltage waveforms, which are the major source of harmonics of system fundamental [5]. Though efforts have been made to reduce harmonics, they still largely exist in ASD systems. These additional harmonics generates a number of extra modulated bearing fault characteristic frequencies present in ASD systems.

Though bearing fault detection studies on line-driven motors that rely on MCSA has been successful, investigation of bearing fault detection on ASD system are still required. Due to significant EMI noise in the stator current of ASD systems and low amplitude bearing fault signatures, it is impossible to detect a bearing fault by simply comparing current spectrum at harmonics of bearing fault characteristic frequencies.

Due to the additional fault characteristic frequency components and the considerable noise level, this study tries to effectively differentiate the healthy and faulty bearings in ASD systems. As an extension to the MCSA, various techniques including wavelet packet decomposition, genetic algorithm, and support vector machine are applied to the stator current in an ASD system to produce a classifier for bearing fault detection at different running speed.

1.2 Proposed Approach

ASD systems have several system characteristics that make bearing fault detection more difficult than line-driven motors. In ASD systems, PWM inverter-fed motor current contains greater number of harmonics resulting from the PWM voltage waveforms. In addition, the EMI floor noise reduces the significance of bearing fault characteristic frequency components in the stator current. With the increasing complexity in detecting defective bearings, an ASD current analysis via wavelet packet decomposition, genetic algorithm, and support vector machine is used to detect ball bearing defects. The current signal from the drive is first sampled at the rate of at least twice that of the carrier frequency of the ASD. The sampled current data is then processed in five steps:

- Suppression of fundamental drive frequency.
- Wavelet packet decomposition.
- Node rms computation.
- Wavelet packet node selection with genetic algorithm.
- Classification with support vector machine.

Each of the following subsections describes each of these steps.

1.2.1 System Fundamental Frequency Suppression

The stator current data is dominated by ASD system harmonics. The system frequency component of the ASD is the fundamental frequency from the inverter that drives the motor. This fundamental frequency is considerably larger than the bearing fault frequency components in magnitude and, therefore, needs to be suppressed before

the current signal is decomposed into wavelet packets. An FFT is run on the current data to determine the fundamental frequency of the PWM inverter output. Then, a second order notch filter is applied to suppress the ASD fundamental harmonic.

1.2.2 Wavelet Packet Decomposition

Wavelet packet decomposition is used to decompose the fundamental-suppressed current data into wavelet packets. Wavelet packet decomposition is implemented as two-channel filter banks with successive filtering and down-sampling. Similar to FFT frequency bins, the resulting wavelet packets are associated with the waveform spectral components. The decomposition is achieved using a special all-pass implementation of elliptic half-band IIR filters. The filter selection was based on better frequency separation and lower computational complexity [6,7,8,9].

1.2.3 rms Computation

After wavelet packet decomposition, each node, which corresponds to a frequency band, contains wavelet packet coefficients (WPC's). The nodes corresponding to the fault characteristic frequencies can then be examined. Wavelet packet coefficients of the nodes can be used to compute the rms values [10]. The rms value of each node reflects the level of the current present in the corresponding frequency band.

1.2.4 Wavelet Packet Node Selection with Genetic Algorithm

The outputs from most ASD inverters are pulse-width modulated (PWM) waveforms. The PWM motor input voltage introduces a larger number of harmonics to ASD's than the sinusoidal voltage in line-driven motors; thus a substantially greater number of the modulated characteristic frequencies in ASD's. This significantly

increases the number of elevated frequency bands from the WPD. Moreover, the characteristic frequency components of defective bearings could contain high level of EMI noise due to the effect of ASD systems. These two factors increases the complexity in the determination of which rms values are to be chosen for comparing good and faulty bearings. Hence, it is more preferable to eliminate nodes that are irrelevant to the detection from classifier finding. The nodes of interest in which the bearing fault characteristic frequencies lie are selected using Genetic Algorithm. Through the GA, a number of sets, called chromosomes, of selected nodes are evaluated by the fitness function. The fitness function for this problem is the percent error in SVM classification. The chromosomes reproduce offspring by recombination and mutation. These new-generation chromosomes are then evaluated. These steps are repeated until convergence.

1.2.5 Classification with Support Vector Machine

The support vector machine (SVM) is a supervised machine learning method for classification. The linear classifiers produced by the SVM are guaranteed to have maximum margins. For linearly non-separable case, the data is mapped into a higher-dimensional space by applying of the kernel trick.

Through each generation of the GA, the SVM computes the fitness of each chromosome. Each fitness is the 10-fold classification error computed by the SVM. The SVM uses the rms values from nodes corresponding to a chromosome to find a classifier and the classifier is evaluated. The percent error of classification for the classifier is the fitness of the chromosome.

In the end, the GA would select the WP nodes that are significant to classifying a bearing fault type at a fundamental frequency for the ASD. The SVM would find the final classifier using the GA-selected WP nodes.

1.3 Organization

Chapter Two consists of two parts. The first part provides the literature review which explains previous works in motor fault detection using MCSA. The second part provides the background information on adjustable speed drives, bearing failures, causes and types of bearing defects, the mechanical and vibrational characteristics resulting from these defects. This part also discusses spectral frequency analysis tools, i.e., short-time Fourier transform and the wavelet theory with emphasis on wavelet packet decomposition, and the supervised machine learning tools, i.e. the genetic algorithm and the support vector machine for classification problems. Also, some background on clustering is presented since it will be compared with the proposed algorithm in classifying healthy and defective current data. In Chapter Three, the detail algorithm of the proposed method is explained. The steps of how signal processing, wavelet packet decomposition, the support vector machine, and the genetic algorithm are provided. In addition, this chapter includes the information of the hardware setup. Chapter Four shows the results from both clustering and the proposed method. The ASD current waveforms at different fundamental frequencies before and after wavelet packet decomposition are depicted. The percent errors of clustering and the proposed method are presented in this chapter. Finally, the conclusion and the future research possibilities are discussed in Chapter Five

CHAPTER 2 BACKGROUND

In this chapter, the literature review and the theoretical background on bearing failures in adjustable speed drives, wavelet theory, the genetic algorithm, and the support vector machine are provided. These should provide a better understanding of the motivation and the underlying theory of the study.

2.1 Literature Review

Previous researches and studies involving fault detection via motor current signature analysis inspire this study to develop a technique for bearing fault detection in adjustable speed drives. Various attempts to detect faults in line driven motors, such as rotor eccentricity, broken rotor bars, and bearing defects have been successful. However, only a very limited number of studies of fault detection in ASD systems have been conducted to date.

Motor Current Signature Analysis, MCSA, was initiated by Oak Ridge National Laboratory [11]. This introduced a non-intrusive means for detecting mechanical and electrical anomalies in both machines and driven equipment. Oak Ridge was seeking a way of assessing the health of reactor cooling pump motors which are located in the reactor containment structure, and thus not accessible to intrusive measurements while the reactor is operational. Since then, the scope of fault detection using MCSA has expanded to include broken rotor bars, insulation faults, and bearing faults, etc.

Kliman demonstrated the relationship between the mechanical vibration and the stator current. [12]. Schoen and Habetler extended a Kliman's equation and showed the relationship of the mechanical bearing vibration to the motor stator current [1]. Yazici and Kliman used the STFT with statistical pattern recognition to detect broken rotor bars and bearing fault in motors. Riley, et. al, authored stator current harmonics and their causal vibrations: a preliminary investigation of sensorless vibration monitoring applications [18, 19]. Zhongming, et. Al, investigated motor mechanical faults, broken rotor bars and rotor eccentricity, through MCSA by wavelet packet decomposition [13]. Eren used wavelet packet decomposition to examine bearing faults in induction motors [6-9].

Bonnett explained the impact of PWM inverter voltage waveforms on AC motors, such as standing waves, the ringing effect, and high level noise contents [14]. Akin, et. al, demonstrated the possibility of detecting bearing faults using the additional harmonics present in PWM inverter-fed ASD systems [5].

2.2 Theoretical Background

Theoretical background on ASD's and their bearing fault characteristics are given the next sections. The information on various techniques, including notch filtering, wavelet packet decomposition, the SVM, the GA, and clustering are also discussed.

2.2.1 Bearing Failures in Adjustable Speed Drives

Adjustable Speed Drives are different from line-driven induction motors. The rotational speed of an ASD can be varied. The input voltage waveform of an ASD is PWM rather than a sinusoid. Thus, the current characteristics of bearing faults in ASD

systems are affected by those differences as well. This chapter provides the background information on Adjustable Speed Drives, the types of bearings, bearing failure causes as well as condition monitoring via MCSA to help better understand the study.

2.2.1.1 Adjustable Speed Drives

An adjustable speed drive system usually consists of an inverter and an induction AC motor. Early ASD's employed six-step and later twelve step waveforms. However, these drives have been largely replaced by the PWM because the substantial amount of low frequency harmonics associated with these drives created additional losses resulting in eddy current heating in both the power system supply transformers and the motor. As these drives have been largely replaced with the more efficient PWM inverters, only these ASD's will be considered in this study. The PWM inverter controls the synchronous speed of the motor and the induction motor rotates at a speed corresponding to input voltage fundamental fed by the inverter.

2.2.1.1.1 AC Induction Motor

Theoretically, the synchronous rotational speed of an AC induction motor is determined by the supplied voltage frequency and the number of poles in the stator windings, which can be described as:

$$RPM = \frac{120 \times f}{p} \tag{2.1}$$

where RPM is the number of revolutions per minute,

f is the frequency of the supplied AC voltage in Hertz,

and p is the number of poles of the machine.

For a line-driven AC machine, the input voltage is from the utility and the input waveform is nearly sinusoidal at a fixed frequency, such as 60 Hz in the United States or 50 Hz in European countries. As a result, most motors can operate only at a relatively constant speeds with the principal variation due to changes in their loads.

An adjustable speed drive also operates under the same principle. However, in the ASD case, the fundamental frequency of the input voltage is no longer fixed. If the fundamental frequency of the input voltage is varied, then the synchronous rotational speed of the motor is also varied proportionally. In this way, the rotational speed of the motor can be adjusted; thus, the term adjustable speed drive.

2.2.1.1.2 Pulse-Width Modulation

To control the rotational speed of an ASD motor via the frequency of the input voltage, a PWM inverter, which is a power electronic conversion device, is used to generate a PWM voltage waveform with a variable fundamental frequency. Ideally, a sinusoidal input voltage is required for a motor. However, a PWM-synthesized waveform yields a performance close to that of a sinusoid. The PWM generates fixed-magnitude pulses with varied duration. The PWM inverter controls the parameters of the output PWM waveform such that the fundamental of the output is of desired magnitude and frequency.

The generation of a PWM waveform involves a periodic (carrier) waveform and another periodic (modulating) waveform of lower frequency. Figure 2.1 illustrates the principle of PWM. A triangular carrier of maximum magnitude V_c is modulated by a sinusoidal waveform $v_m(\omega,t) = V_m \sin(\omega t)$. The intersections of both waveforms

determine the duration of the modulated pulses. The magnitude of the output pulses is constant.

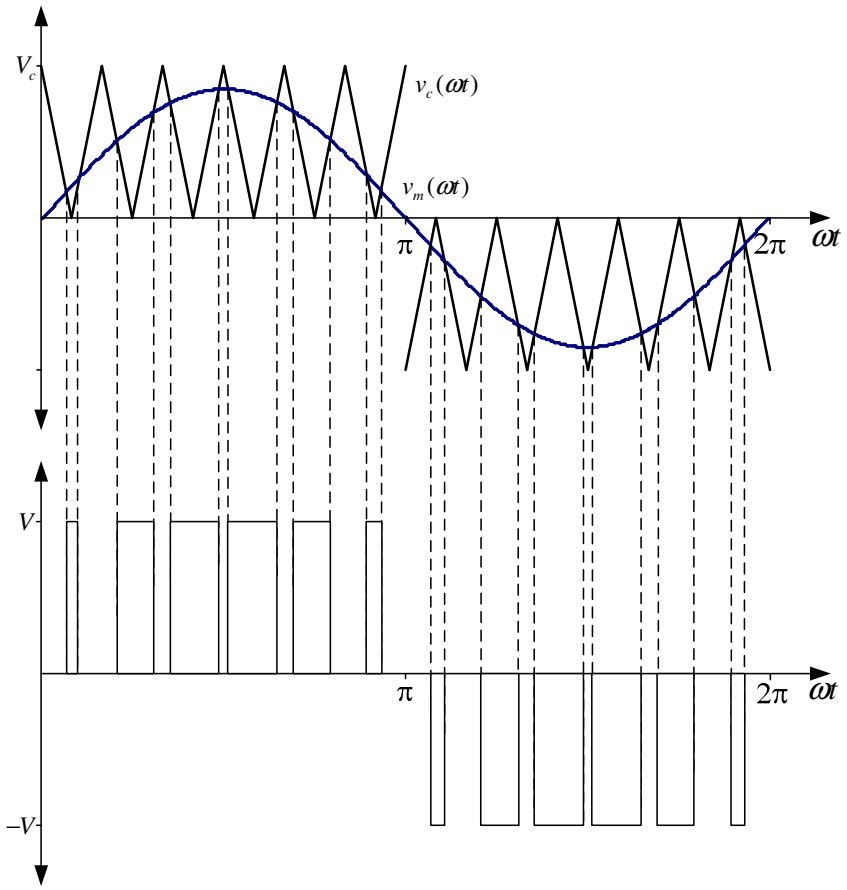

Figure 2.1. Principle of pulse width modulation

As one can see, the dominant frequency of the modulated pulses is located around that of the carrier frequency. This, however, is filtered out by the lowpass filter action of the motor's series inductance. As a result, the pulsations are removed and the fundamental of the modulating frequency becomes governing and is the dominant frequency driving the motor.

The PWM input voltage also introduces harmonics k of the modulated waveform into the system. The harmonics k involve the following quantities: The modulation index or modulation ratio, M, and the carrier ratio or the frequency ratio, p.

$$M = \frac{V_m}{V_c} \tag{2.2}$$

$$p = \frac{\text{frequency of carrier wave}}{\text{frequency of modulating wave}} \tag{2.3}$$

The harmonics k of the modulated waveform are given by

$$k = l\,p \pm n \tag{2.4}$$

where l is the carrier harmonic order and n is the carrier side-band.

However, the harmonic magnitudes are independent of p when $p > 9$ [15]. That is, for $p > 9$, the harmonics k are reduced to

$$k = n \tag{2.5}$$

By varying the frequency of the modulating waveform, the frequency of the PWM inverter output can be controlled and, in turn, controls the rotational speed of the drive.

2.2.1.2 Bearing Types

A bearing is a device that reduces friction and at the same time allows constrained relative motion between two parts of a machine. Rotational bearings can be classified by their loads into two types: thrust and radial. In a thrust bearing, the loads are axial. A swivel stool is a typical application of this type of bearing. The load is the weight of the person sitting on the stool. The other type is designed to sustain radial loads, such as

those in electric motor shafts supplying the belt driven loads. There is also the combination of thrust and radial bearings, which are commonly used in the axel wheel bearings of cars.

Electric motors typically use redial-load bearings at both shaft and opposite ends. They can be sleeve and/or rolling-element bearings. Sleeve bearings are simply the shaft and the hole possibly with lubricant. They are mainly integrated in large and high-speed machines. They have nearly infinite lifetime, produce less vibration and noise, and are less sensitive to external vibrations, better axial play, and easier accessibility [16]. Sleeve bearings of sintered bronze impregnated with oil are employed lower cost machines where they have a limited lifetime and are usually not replaceable. Sleeve bearings of sintered bronze impregnated with oil are employed lower cost machines where they have a limited lifetime and are usually not replaceable. Rolling-element bearings are used in virtually all small to medium sized motors [17]. Their advantages over sleeve bearings include exact shaft guiding, lower start-up torque, and fewer leakage and maintenance problems [6].

Rolling-element bearings utilize two types of rolling elements: balls and rollers. In a ball bearing, the contacts of each ball between the inner and outer races are very small, which result in smooth operations. However, this small contact area reduces their ability to support heavy loads. The balls can fail easily if the bearing is overloaded. In a roller bearing, the rollers are cylindrical and provide more contact area between the inner and outer races. This allows the bearing to handle larger loads.

2.2.1.3 Bearing Failure Causes

In electrical motors, rolling-element bearings usually undergo three major modes of bearing failure: abrasion, fatigue, and pressure-induced welding. Abrasion occurs when the bearing material is eroded by contaminants. Fatigue happens when the material is repeatedly strained and released and eventually breaks. Pressure-induced welding occurs when two pieces of metal are pressed and welded together by a very high pressure. Other kinds of failure causes, such as vibration, insufficient/contaminated lubricant, misalignment, and brinelling, eventually become one or more of the three major causes.

The life of a bearing in motors can be predicted using life rating L10 [6]. L10 is the life n millions of revolutions that 90 percent of the identical bearings will complete or exceed. L10 is described by

$$L10 = \frac{10^6}{60n}\left(\frac{C}{P}\right)^a \tag{2.6}$$

where a = 3 for ball bearings and a = 10/3 for roller bearings

n = rotation speed in RPM, C = Bearing Dynamic Load rating

P = load

Most bearings do not reach their expected lifetime due to several reasons. Poor lubrication is the most significant reason that leads to early bearing failures. Also, some bearings are replaced too soon since the cost to replace them is inexpensive. Contamination and abuse are the other reasons.

In addition to the mechanical failure causes mentioned, motors in ASD systems may experience electrical effects from the PWM source that further reduce the lives of

their bearings. Electrical discharge machining (EDM) resulting from arcing causes microscopic pits on the inner and outer races of the motor. Imbalances in the phase winding capacitances between the stator and the rotor put the rotor at a potential relative to ground. The potential is increased by the high current through this small capacitance because of the high dv/dt of the PWM waveform. If you think of a wye connection if the legs of the wye are balanced and the supply is balanced the center point of the wye is ground for a grounded wye supply. However if the wye capacitance is imbalanced the potential of the center point of the wye is pulled toward the phase(s) with the highest capacitance. Thus the rotor has a potential relative to the grounded frame of the machine. This potential appears across the bearing elements and results in the current the produces the EDM machining, which essentially damages the bearings. This introduces more vibration and abrasion to the bearings. Moreover, in motors in ASD's with PWM inverters, high dv/dt current flowing through capacitance formed by the races, lubricant film, and bearing balls can entirely change the chemical composition of lubricant. When the lubricant loses its property, the bearings could fail catastrophically.

2.2.1.4 Condition Monitoring via Vibration Analysis

Monitoring via mechanical vibration is a widely used method to monitor the condition of a machine. Defects on a machine normally introduce unbalanced operation causing characteristic vibrations. The vibration and motor current are studied [18,19] and are found to be directly related.

2.2.1.5 Condition Monitoring via MCSA

Motor Current Signature Analysis (MCSA) is a method for monitoring machinery in the industry by means of its electrical currents. It is based on the fact that the physical condition of an operating motor affects its mechanical characteristics. Those characteristic changes, such as air gap flux density, change the machine inductances and, in turn modify the electrical current passing through the motor. The condition of the motor can be assessed by analyzing the current data. Since a motor rotates, the resulting vibrations are periodic and defect conditions usually show as recognizable frequency patterns related to the machines angular speed. MCSA can be used to diagnose problems in electrical motors such as cracked or broken rotor bars, rotor eccentricity, and bearing wear.

2.2.1.6 Cracked or Broken Rotor Bars

Cracked or broken rotor bars prevent the current from flowing in the rotor bar. This type of faults introduces spectral components into the stator current. As a result, the cracked and broken rotor bars can be detected by analyzing the current spectrum near the broken rotor bar fault frequency, f_{RB}, which can be formulated as

$$f_{RB} = f_e \left[\left(\frac{k}{p} \right) (1 - s) \pm s \right] \tag{2.7}$$

where

k = harmonic index ($k = 1, 2, 3, \ldots$)
s = per unit slip
p = number of fundermental pole-pairs
f_e = power supply frequency

Due to the structure of the windings in a motor, only the frequency component with harmonics $k = 1, 5, 7, 11, 13, \text{etc.}$ will appear in the current. Then, the equation can be rewritten as

$$f_{RB} = f_e \left[1 \pm 2ks\right] \tag{2.8}$$

The frequency components resulting from cracked or broken rotor bar are very close to the fundamental. As a result, it is very difficult to detect this type of faults. Some other techniques to detect such faults include analysis of motor starting current and analysis of the stator-induced voltage after the power supply removal.

2.2.1.7 Rotor Eccentricity

Rotor eccentricity occurs when the rotor is unbalance or is misaligned. As the rotor rotates, it creates a point of minimum air gap at the frequency of rotation. The following equation describes the rotor eccentricity frequency f_{RE}

$$f_{RE} = f_e \left[\left(\frac{k}{p/2} \right) (1 - s) \pm 1 \right] \tag{2.9}$$

where

k = harmonic index ($k = 1, 2, 3, \ldots$)
s = per unit slip
p = number of fundermental pole-pairs
f_e = power supply frequency

The spectral magnitude of the above frequency of rotor eccentricity can be used to detect rotor unbalance and misalignment. The rotor unbalance is at $1\times$ rotational speed while misalignment appears as $1\times$ and $2\times$ rotational speed components.

2.2.1.8 Bearing Faults

Bearing faults are the major causes of motor failures. In ASD systems, bearings are more likely to be damaged from the highly accelerated/decelerated operation and the effects of electrical discharge machining resulting from high dv/dt, which are introduced by PWM input voltage. When a bearing fault occurs, the mechanical damage causes the machine to vibrate at a frequency corresponding to the bearing fault type. Four major types of bearing faults are inner race, outer race, cage, and ball defects. Early stage in the bearing failure, the vibration frequency is distinctive and later it gets buried in the noise as the fault advances [20]. This makes it more difficult to detect long-running faults.

The important geometric properties of a ball bearing include the number of balls, each ball's diameter, and the pitch diameter. The pitch diameter is the diameter of the circle with a circumference that goes through the center of every ball. Figure 2.2 displays the geometry of a typical ball bearing.

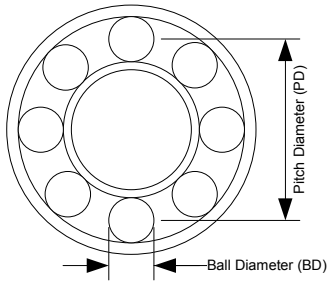

Figure 2.2. Ball bearing geometry

Given the rotor speed and bearing dimensions, the vibration frequency of each bearing fault type can be determined. In the following subsections, the vibration frequency of each bearing faults is presented.

2.2.1.8.1 Cage Defect

The bearing cage of a ball bearing is a device that retains and separates the balls at equal distances. It also retains the balls to roll along the raceways. When the motor is running, the cage turns at a linear velocity, which is the mean of the inner and outer race linear velocities. The cage linear velocity can be used to compute the fundamental cage defect, f_{CD}.

$$w_{CD} = \frac{V_c}{r_c} = \frac{V_i + V_o}{D_c} \tag{2.10}$$

where

w_{CD} = frequency of the inner race in Hertz
V_c = velocity of the cage
r_c = raduis of the cage
V_i = velocity of the inner race
V_o = velocity of the outer race
D_c = diameter of the cage

$$f_{CD} = \frac{f_i r_i + f_o r_o}{PD} = \frac{1}{PD}\left(f_i \frac{PD - BD\cos\theta}{2} + f_o \frac{PD + BD\cos\theta}{2} \right) \tag{2.11}$$

where

f_i = frequency of the inner race in Hertz
r_i = radius of the inner race
f_o = frequency of the outer race in Hertz
r_o = radius of the outer race
PD = pitch diameter
BD = ball diameter
θ = contact angle of the ball

For motors, the housing is stationary and the outer race is mounted to the housing. That is, the outer race is also relatively stationary. The inner race and the shaft are installed together and both rotate at the same angular speed. As a result, it can be assumed the following.

$$f_o = 0 \text{ and } f_i = f_{rm} \tag{2.12}$$

where f_{rm} is the mechanical rotor speed in Hertz.

Equation 2.11 can be rewritten as

$$f_{CD} = \frac{1}{2} f_{rm}(1 - \frac{BD}{PD}\cos\theta) \tag{2.13}$$

Most bearing geometric data can be obtained from the manufacturer. However, when such data is not available, the f_{CD} can be approximated for most ball bearings with 6 to 12 balls by

$$f_{CD} = 0.4 f_{rm} \tag{2.14}$$

2.2.1.8.2 Inner Race Defect

The inner race defect frequency, f_{ID}, is associated with the rate at which bearing balls traverse a defect point on the inner race. Each ball passes the defect point at the frequency difference of cage and inner race. Since there are n balls, the frequency is linearly proportional to the number of balls. The fundamental frequency of the inner race defect, then, can be computed as

$$f_{ID} = n\left|f_{CD} - f_i\right| \tag{2.15}$$

Expanding Equation 2.15,

$$f_{ID} = n\left|\frac{f_i r_i + f_o r_o}{PD} - f_i\right|$$
$$= n\left|\frac{f_i(r_c - \frac{BD\cos\theta}{2}) + f_o(r_c + \frac{BD\cos\theta}{2})}{PD} - f_i\right| \quad (2.16)$$
$$= \frac{n}{2}\left|(f_i - f_o)(1 + \frac{BD\cos\theta}{2})\right|$$

Substituting $f_o = 0$ and $f_i = f_{rm}$ from Equation 2.12, f_{ID} becomes

$$f_{ID} = \frac{n}{2} f_{rm}(1 + \frac{BD}{PD}\cos\theta) \quad (2.17)$$

The f_{ID} can be approximated for most ball bearings with 6 to 12 balls by

$$f_{ID} = 0.6\, n\, f_{rm} \quad 2.18$$

2.2.1.8.3 Outer Race Defect

Similar to f_{ID}, The outer race defect frequency, f_{OD}, is associated with the rate at which bearing balls traverse a defect point on the outer race. Each ball passes the defect point at the frequency difference of cage and outer race. Since there are n balls, the frequency is linearly proportional to the number of balls. The fundamental frequency of the outer race defect, then, can be computed as

$$f_{OD} = n\left|f_{CD} - f_o\right| \quad (2.19)$$

Expanding Equation 2.19,

$$
\begin{aligned}
f_{OD} &= n\left|\frac{f_i r_i + f_o r_o}{PD} - f_o\right| \\
&= n\left|\frac{f_i(r_c - \frac{BD\cos\theta}{2}) + f_o(r_c + \frac{BD\cos\theta}{2})}{PD} - f_o\right| \\
&= \frac{n}{2}\left|(f_i - f_o)(1 - \frac{BD\cos\theta}{2})\right|
\end{aligned}
\tag{2.20}
$$

Substituting $f_o = 0$ and $f_i = f_{rm}$ from Equation 2.12, f_{OD} becomes

$$f_{OD} = \frac{n}{2} f_{rm}(1 - \frac{BD}{PD}\cos\theta) \tag{2.21}$$

The f_{OD} can be approximated for most ball bearings with 6 to 12 balls by

$$f_{OD} = 0.4\, n\, f_{rm} \tag{2.22}$$

2.2.1.8.4 Ball Defect

The fundamental ball defect frequency, f_{BD}, results from the rotation of the ball about its own axis through its center. The ball defect frequency can be formulated as

$$
\begin{aligned}
f_{BD} &= \left|(f_i - f_{CD})\frac{r_i}{r_b}\right| = \left|(f_o - f_{CD})\frac{r_o}{r_b}\right| \\
&= \frac{PD}{2BD}\left|(f_i - f_o)(1 - \frac{BD^2\cos^2\theta}{PD^2})\right|
\end{aligned}
\tag{2.23}
$$

Substituting $f_o = 0$ and $f_i = f_{rm}$ from Equation 2.12, f_{BD} becomes

$$f_{BD} = \frac{PD}{2BD} f_{rm}(1 - \frac{BD^2\cos^2\theta}{PD^2}) \tag{2.24}$$

2.2.1.9 Characteristic Frequencies

Bearing faults create mechanical vibration with fundamental frequency presented in the previous section. These mechanical vibrations result in air gap eccentricity which subsequently produces anomalies in the air gap flux density. The changes in the flux density affect the machine inductances causing stator current distortion at the vibrational harmonics. For line-driven motors, the characteristic current frequencies, f_{CF}, due to characteristic vibration frequencies are computed by

$$f_{CF} = \left| f_e \pm m f_v \right| \tag{2.25}$$

where

f_e = power supply frequency in Hertz
f_v = vibration frequency in Hertz
m = vibration modulation index

In the case of the ASD, the supply to the motor is a PWM voltage waveform. Recalling the harmonic index of PWM inverters from Equation 2.5, a PWM waveform contains harmonics $k = n$ of the fundamental frequency. The power supply for the ASD, $f_{e,ASD}$ is composed chiefly of the n odd harmonics of the fundamental drive frequency, f_f. That is,

$$f_{e,ASD} = n f_f \tag{2.26}$$

Thus, the characteristic current frequency of the ASD can be written as

$$f_{CF,ASD} = \left| n f_f \pm m f_v \right| \tag{2.27}$$

where

f_f = fundamental supply frequency in Hertz
f_v = vibration frequency in Hertz
n = PWM harmonic index of fundamental supply
m = vibration modulation index

As a result, an ASD system with a bearing defect produces the characteristic current frequency components that contain n times as many harmonics as a line driven motor with a bearing defect.

2.2.2 Wavelet Theory

Wavelet theory has been used widely in various fields such as mathematics, physics, sciences, and engineering. Since its introduction, it has been adopted for a great number of applications. In electrical and computer engineering and computer science areas, the wavelet transform (WT) is used in signal processing, speech recognition, computer graphics, computer vision, data compression, and data analysis. The wavelet transform has been replacing the Fourier transform, especially in non-stationary processing. Wavelet Packet Decomposition (WPD) is an extension to wavelet theory which yields finer frequency resolution.

In this chapter, the Short-Time Fourier Transform (STFT) and wavelet theory will be reviewed. Wavelets, multi-resolution analysis, and sub-band coding, and wavelet packet analysis will be discussed as well.

2.2.2.1 Short Time Fourier Transform

The Fourier transform (FT) is widely used in spectral analysis. It decomposes a signal into a continuous spectrum of frequency components. The use of FT has been limited to stationary signals—signals with no abrupt change—due to the infinite extent of the integral. In other words, FT only illustrates the overall spectrum with less time locality information. Equation 2.28 describes the Fourier transform of function $x(t)$.

$$FT\{x(t)\} \equiv X(f) = \int_{-\infty}^{\infty} x(t) e^{-j2\pi ft} dt \tag{2.28}$$

Due to FT time locality property, it is impossible to decompose a signal and look at the change over time with FT. As a result, Short-Time Fourier Transform (STFT) has

been introduced to determine the sinusoidal frequency and phase content of local sections of a signal as it changes over time.

$$STFT\{x(t)\} \equiv X(\tau, f) = \int_{-\infty}^{\infty} x(t)w(t-\tau)e^{-j2\pi ft}dt \tag{2.29}$$

where $w(t)$ is a window function

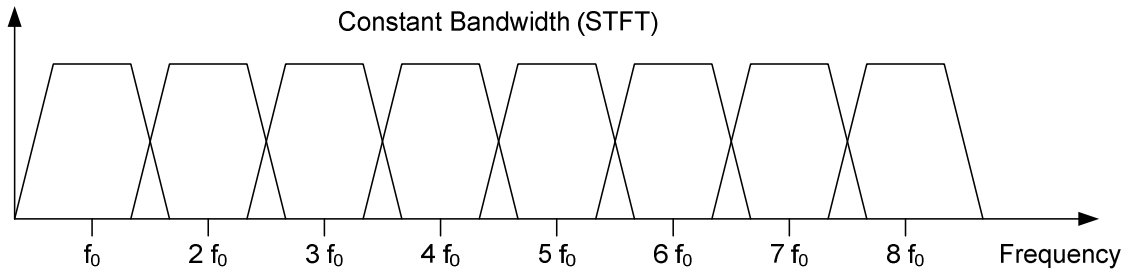

Figure 2.3. The frequency separation of analysis filter in STFT

In STFT, the size of window is fixed. If the transient signal energy is within the window, then STFT can produce a valid result. However, transients longer than the window can be separated and significant frequency information may be lost. A wider window yields better frequency resolution, but inferior time resolution. A narrow window yields poor frequency resolution, but good time resolution. Given window function $w(t)$ and its Fourier transform $W(f)$, Equations (2.30) and (2.31) describe the frequency bandwidth and time spread, respectively. Δf and Δt are frequency and time resolutions, respectively.

$$\Delta f^2 = \frac{\int f^2 |W(f)|^2 df}{\int |W(f)|^2 df} \tag{2.30}$$

$$\Delta t^2 = \frac{\int t^2 |w(t)|^2 dt}{\int |w(t)|^2 dt} \tag{2.31}$$

This property is related to the Heisenberg inequality (uncertainty principle). It is impossible to have both high frequency and time resolution. There must be a balance between the two. The product of frequency and time resolution has a lower limit.

$$\Delta t \Delta f \geq \frac{1}{4\pi} \tag{2.32}$$

The shortcoming of the STFT is in the analysis of non-stationary signals. Frequency and time resolution must be well compromised since transients needs be located and long-term behavior needs be identified. Often, such compromise is impossible due to the nature of non-stationary signals.

2.2.2.2 Continuous Wavelet Transform

The wavelet transform is more suitable for non-stationary signal processing. It is a new approach to overcome the resolution problem in STFT by decomposing a signal into time/frequency space simultaneously. A signal is represented by a finite length or fast decaying oscillating waveform called the mother wavelet $\psi(t)$. The mother wavelet is scaled and translated to match the signal. Child wavelets can be obtain from the mother wavelet by

$$\psi_{a,b}(t) = \frac{1}{\sqrt{a}} \psi(\frac{t-b}{a}) \tag{2.33}$$

Scale a is positive and b defines the translation or shift. The continuous wavelet coefficients are defined as

$$CWT_x^{\psi}(a,b) = \langle x, \psi_{a,b} \rangle = \int x(t) \psi_{a,b}^*(t) dt \tag{2.34}$$

2.2.2.3 Discrete Wavelet Transform

Wavelets can be discretized by replacing scaling and translating parameters as follows.

$$a = a_0^j \text{ and } b = kb_0a_0^j \tag{2.35}$$

Equation (2.33) them becomes

$$\psi_{a,b}(t) = a_0^{-j/2}\psi(a_0^{-j}t - kb_0) \tag{2.36}$$

Usually, $a_0 = 2$ and $b_0 = 1$ are chosen for dyadic sampling and decomposition. If a perfect reconstruction is required, the mother wavelet must be an orthogonal basis, which must satisfy

$$\langle \psi_{j,k}(t), \psi_{m,n}(t) \rangle = \begin{cases} 1, & j = m \text{ and } k = n \\ 0, & \text{otherwise} \end{cases} \tag{2.37}$$

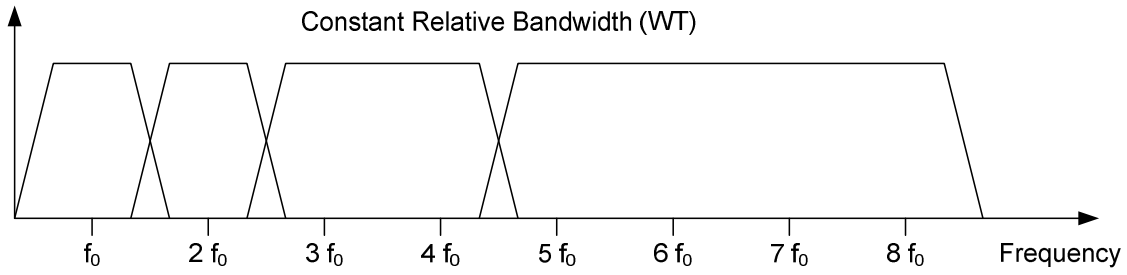

Figure 2.4. The frequency separation of analysis filter bank in WT

The Discrete Wavelet Transform decomposes a signal into logarithmically spaced frequency components as shown in Figure 2.4. High frequency components have finer time resolution, but coarser frequency resolution. On the contrary, low frequency components have coarser time resolution, but finer frequency resolution.

2.2.2.4 Multiresolution Analysis

Multiresolution analysis was introduced by Mallat and Meyer. Daubechies demonstrated the relation between Multiresolution analysis and wavelet bases. Multiresolution analysis can be viewed as decomposition of a signal into a smooth background and fluctuations or details.

At level $j = J$, the scale is unity and at level j, the scale is 2^{-j}. For each level j, the next level of resolution is $j-1$. At a new resolution level, $f_{j-1}(t)$ is decomposed into a smooth part $f_j(t)$ and the details $d_j(t)$.

$$f_{j-1}(t) = f_j(t) + d_j(t) \tag{2.38}$$

The signal $f(t)$ can then be written as

$$f(t) = f_j(t) + \sum_{k=j}^{\infty} d_k(t) \tag{2.39}$$

The space of the signal is square integrable, $L^2(\mathbb{R})$, is composed of a sequence of subspaces $\{W_k\}$ and V_j. $f_j(t)$ is in subspace V_j and $d_k(t)$ are in subspace W_k. From Equation (2.38), subspaces can also be decomposed as follows

$$V_{j-1} = V_j \oplus W_j \tag{2.40}$$

where $V_j \perp W_j \quad \forall j \in \mathbb{Z}$

The decomposition can be done further such that

$$V_{j-1} = W_j \oplus V_j = W_j \oplus W_{j+1} \oplus V_{j+1} = \cdots = W_j \oplus W_{j+1} \oplus W_{j+2} \oplus \cdots \oplus W_J \oplus V_J \tag{2.41}$$

A nested sequence $\{V_j\}_{j\in\mathbb{Z}}$ is a multiresolution analysis of $L^2(\mathbb{R})$ if the following requirements are satisfied.

i) $$\cdots \subset V_j \subset V_{j-1} \subset \cdots \subset V_1 \subset V_0 \subset V_{-1} \subset \cdots \subset L^2(\mathbb{R}) \tag{2.42}$$

ii) $$\bigcap_j V_j = \{0\}, \quad \overline{\bigcap_j V_j} = L^2(\mathbb{R}) \tag{2.43}$$

iii) $$f(t) \in V_j \Leftrightarrow f(\frac{t}{2}) \in V_{j+1} \tag{2.44}$$

iv) $$f(t) \in V_j \Rightarrow f(t-2^j k) \in V_j \tag{2.45}$$

v) There exists the scaling function $\phi(t)$ such that $\phi(t-k)$ is an orthonormal basis of V_0. (2.46)

An orthogonal basis of subspace V_j can be formed by dilating and translating the scaling function ϕ of a multiresolution analysis.

$$\phi_{j,k}(t) = 2^{-j/2}\phi(2^{-j}t - k) \tag{2.47}$$

2.2.2.5 Sub-band Filtering Schemes

Daubechies has demonstrated that the wavelet transform can be achieved by using multirate filter banks. Lowpass and highpass filters, which are quadrature mirror filters, are used for two-channel analysis. Figure 2.5 shows the wavelet analysis filter bank with lowpass, h^*_{-k}, and highpass, g^*_{-k}, filters.

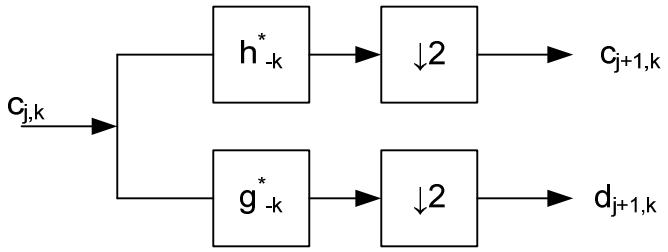

Figure 2.5. Two-band analysis filter bank

The perfect reconstruction of the analyzed signal can be recovered with the synthesis filter bank. The relationship between the lowpass and highpass filters is defined by

$$g_k = -1^k h_{-k+1} \tag{2.48}$$

Figure 2.6 illustrates the two-band synthesis filter bank which is used to reconstruct the signal.

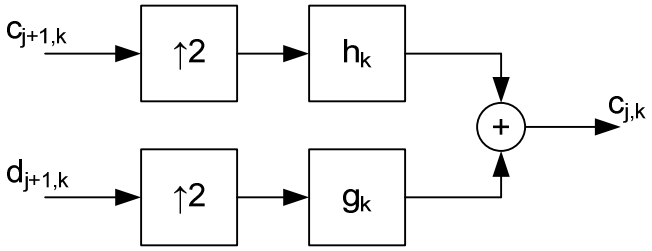

Figure 2.6. Two-band synthesis filter bank

The decomposition using two-band filter bank is dyadic. The signal is decomposed into low and high frequency components. The output from the lowpass filter is then fed as the input into the filter bank. This is done recursively so that the decomposition is dyadic as shown in Figure 2.7.

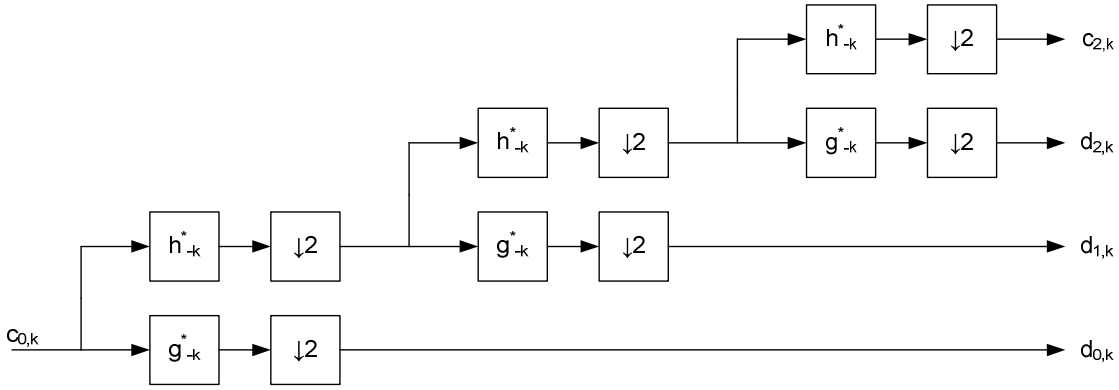

Figure 2.7. Dyadic wavelet decomposition filter bank

The wavelet coefficients for level j can be computed from the scaling coefficients form level $j-1$ as shown in Equations 2.49 and 2.50.

$$\psi_{j,k}(x) = \sum_n g_{n-2k}\phi_{j-1,n}(x) \tag{2.49}$$

$$\left\langle f, \psi_{j,k} \right\rangle = \sum_n \overline{g_{n-2k}} \left\langle f, \phi_{j-1,n} \right\rangle \tag{2.50}$$

The scaling coefficients for level j can be computed from the scaling coefficients form level $j-1$ as follows.

$$\phi_{j,k}(x) = \sum_x h_{n-2k}\phi_{j-1,n}(x) \tag{2.51}$$

$$\left\langle f, \phi_{j,k} \right\rangle = \sum_n \overline{h_{n-2k}} \left\langle f, \phi_{j-1,n} \right\rangle \tag{2.52}$$

This process can be repeated until the desired level J is reached.

2.2.2.6 Wavelet Packet Decomposition

The wavelet packets generalize the link between multiresolution analysis and wavelets. It provides better time localization for higher frequencies in exchange for poor frequency resolution. The wavelet packet was introduced by Coifman, Meyer, and Wickerhauser. The idea of wavelet packet decomposition is that a two-channel filter bank is applied to both the scaling coefficients and the wavelet coefficients. The frequency separation from the wavelet packet decomposition is very similar to that of STFT as depicted in Figure 2.8.

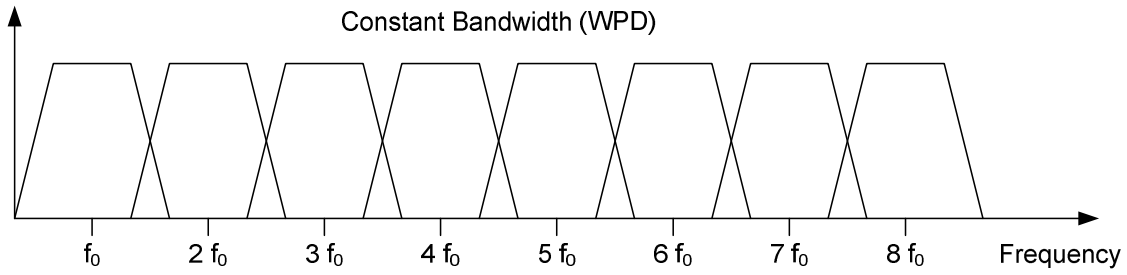

Figure 2.8. Frequency separation by WPD

Theorem (Coifman, Meyer, Wickerhauser) [21] Let $\{\theta_j(t-2^j n)\}_{n\in\mathbb{Z}}$ be an orthonormal basis of a space $\mathbf{U}j$. Let h and g be a pair of conjugate mirror filters. Define

$$\theta^0_{j+1}(t)=\sum_{n=-\infty}^{+\infty} h[n]\theta_j(t-2^j n) \text{ and } \theta^1_{j+1}(t)=\sum_{n=-\infty}^{+\infty} g[n]\theta_j(t-2^j n) \tag{2.53}$$

The family is

$$\left\{\theta^0_{j+1}(t-2^{j+1}n),\theta^1_{j+1}(t-2^{j+1}n)\right\}_{n\in\mathbb{Z}} \tag{2.54}$$

The theorem reveals that, setting $\mathbf{U}j=\mathbf{W}j$, new bases can be derived by dividing the detail spaces. Vector spaces can be recursively split and represented in a binary tree. Space $\mathbf{W}_j^p$ denotes space at level j and node p.

Wavelet packet decomposition yields the wavelet packet coefficients, $d^p_{j,k}$, of node (j,p). The coefficients for odd and even nodes are described in Equations (2.55) and (2.56), respectively.

$$d^{2p}_{j+1,k}=d^p_{j,k}*\bar{h}(2k) \tag{2.55}$$

$$d^{2p+1}_{j+1,k}=d^p_{j,k}*\bar{g}(2k) \tag{2.56}$$

It is very important to note that the frequency order of the wavelet decomposed results is not in increasing frequency order. However, they are in sequential binary gray code order.

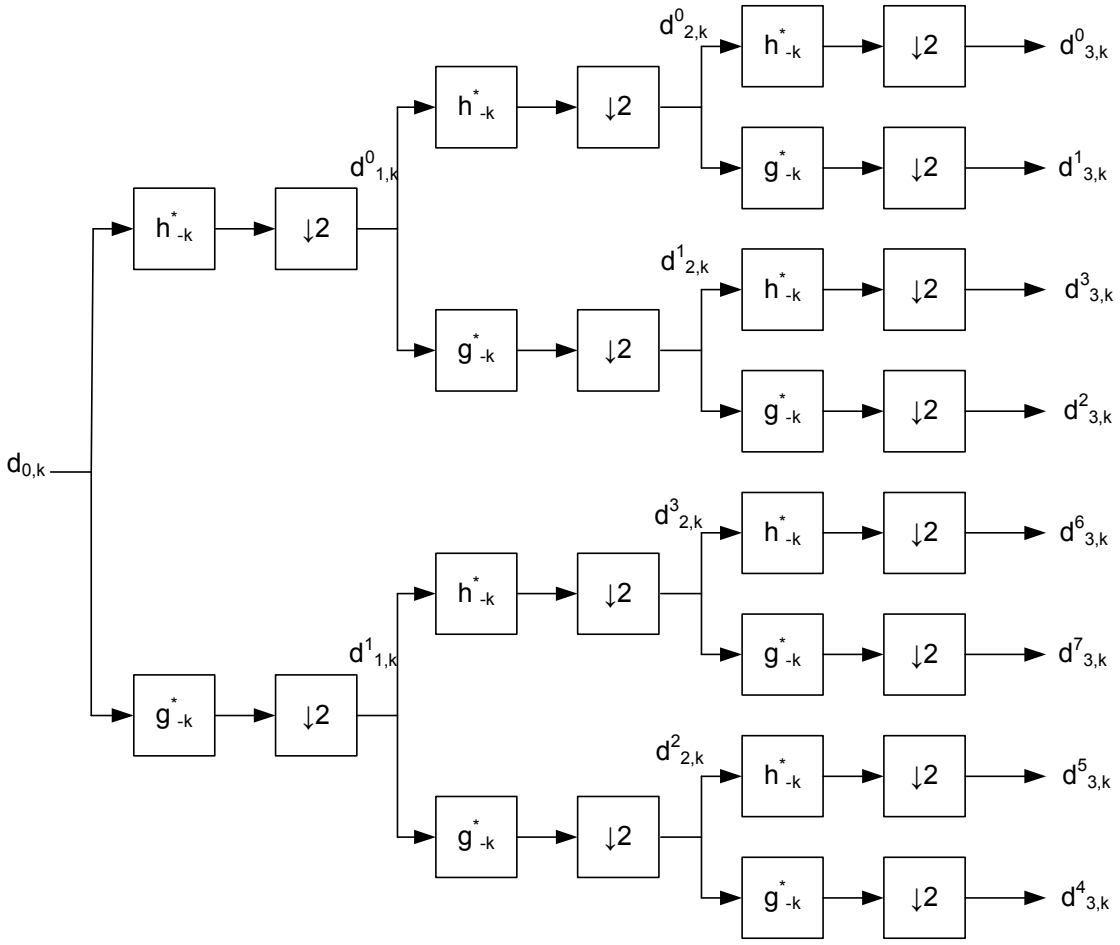

Figure 2.9. Wavelet Packet Decomposition via two-channel filter banks

The WP coefficients obtained from the above equations can be used to compute the rms value of each corresponding node as described in Equation (2.57).

$$x_{rms}(j,p) = \sqrt{\frac{1}{K}\sum_{k}(d_{j,k}^{p})^{2}} \tag{2.57}$$

The total rms value for depth j can be computed by

$$x_{rms}(j) = \sqrt{\frac{1}{P}\sum_{p} x_{rms}^{2}(j,p)} \tag{2.58}$$

2.2.3 Genetic Algorithm

The Genetic Algorithm (GA) is a technique to obtain approximate or exact solutions to optimization problems. It was first introduced by John Holland in 1975 [22]. The GA is a class of Evolutionary Computation and is classified as global optimization heuristics. The solutions to an optimization in the GA are achieved by a series of the reproduction (crossover and mutation) and selection of the chromosomes (solution candidates) from the previous generations.

These problems can be hard-to-solve problems such as traveling salesman prolem (TSP) or optimization problems such as finding Black Jack's best strategy. Chromosomes are the representations of tentative solutions which can be evaluated by a Fitness function. Fitness function determines how fit a chromosome is. These chromosomes undergo genetic operations—selection, crossover or reproduction, and mutation—to produce next-generation chromosomes. This occurs repeatedly until chromosomes of acceptable solutions are discovered or time eventually runs out.

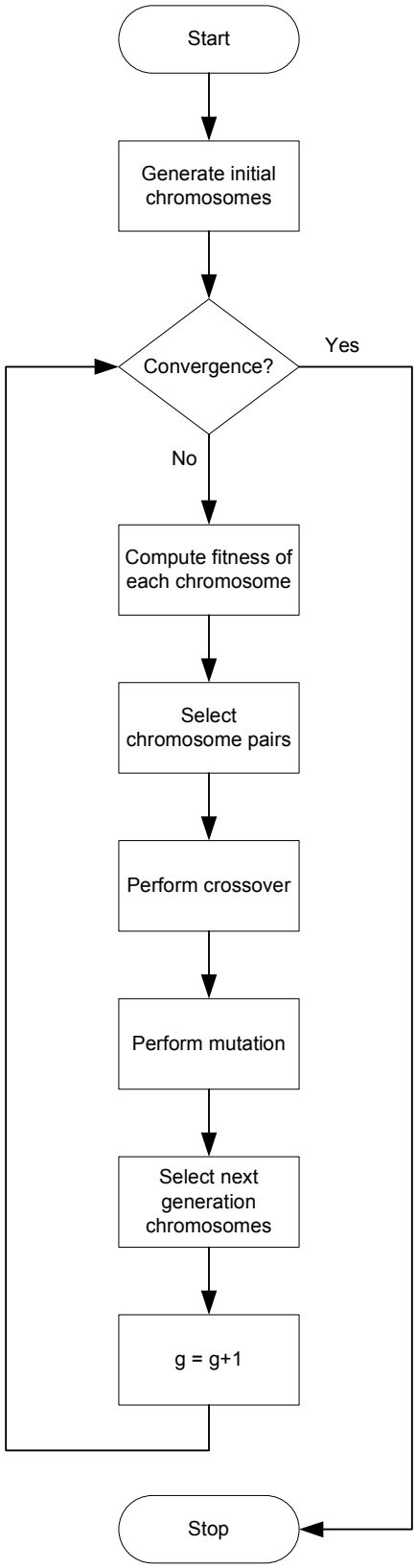

Figure 2.10 Flowchart of a typical genetic algorhim

2.2.3.1 Genetic Algorithm Pseudocode

The pseudocode of a general GA can be summarized as follows:

1: Let generation $g \leftarrow 0$.

2: Initialize the initial generation set of chromosomes $C_g = \{\vec{C}_{g,n} \mid n = 1, \ldots, N\}$, where $\vec{C}_{g,n}$ is a vector of I variables and represents a candidate solution at generation g.

3: Evaluate the fitness of each individual $\vec{C}_{g,n} \in C_g$.

4: While (no convergence)

5: $g \leftarrow g + 1$.

6: Select parents from C_{g-1} and reproduce offspring O_g via crossover of the selected parents.

7: Mutate offspring in O_g.

8: Select the new generation C_g from the previous generation C_{g-1} (elites) and the offspring O_g.

9: Evaluate the fitness of each individual $\vec{C}_{g,n} \in C_g$.

10: Check for convergence.

11: End while

2.2.3.2 Chromosome Representation

The GA utilizes a population of chromosomes, each of which represents a candidate solution to the problem. A chromosome is composed of genes, which allow inheritance to function. Each gene represents a variable in the solution. For example, in the traveling salesman problem (TSP), a chromosome consists of a number of genes

equal to the number of cities. A gene is the city identification. The order of genes in a chromosome indicates the order of the cities to visit.

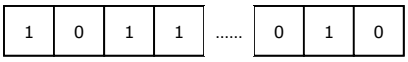

Figure 2.11 A chromosome in a genetic algorithm

In the case of I binary variables, a chromosomes represents a binary vector (or bit string) of fixed length. Each bit represents each binary variable and the length of the bit string is equal to the number of the binary variables.

In the case of an integer or continuous-valued variables, each variable can be encoded as a D-bit vector. These vectors are concatenated to form a bit string, i.e. a chromosome. The length of the bit string is greater than the number of variables.

2.2.3.3 Crossover

A crossover in the GA is a genetic operator to reproduce offspring from a pair of chosen chromosomes. The crossover is achieved by recombining two chromosomes. Parent chromosomes are chosen from the population in the current generation. Random parts of the chosen chromosome pair are exchanged to form the offspring pair.

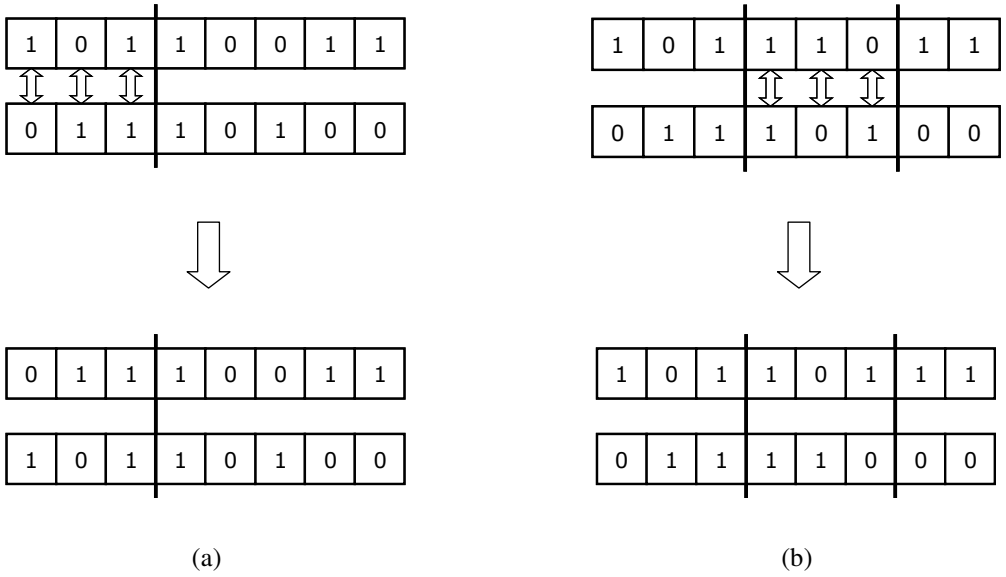

Figure 2.12 One-point crossover (a) and two-point crossover (b)

For the fixed length chromosomes, there are two types of crossover techniques

One-point Crossover A crossover point is selected. All genes beyond that point are swapped between the two parents.

Two-point Crossover Two crossover points are selected. All genes between the points are swapped between the two parents.

2.2.3.4 Mutation

Mutation is a genetic operator that randomly changes some genes in a chromosome in order to maintain genetic diversity. Possibly, chromosomes in the population can become very similar. A crossover on these chromosomes may not introduce new distinct solutions; thus, local extrema. Mutation avoids this from happening by randomly changing some genes. This increases the distinctiveness of chromosomes and allows chromosomes to skip the local extrema.

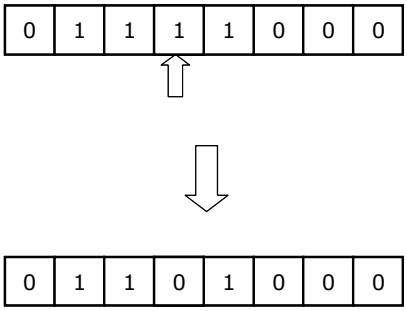

Figure 2.13 Mutation

2.2.4 Support Vector Machine

The Support Vector Machine (SVM) is a new approach in supervised machine learning methods, which can be used in classification and regression. In this study, the focus is on finding classifiers. For a linearly separable data set, the SVM provides the optimal linear decision boundary. In other words, the SVM yields a hyperplane that with maximum margins for a given two-class data set. The SVM can also discover a non-linear decision boundary that separates the data effectively. In the non-linear case, this is done by the kernel trick, a mapping of the data into a higher dimensional space by means of a kernel.

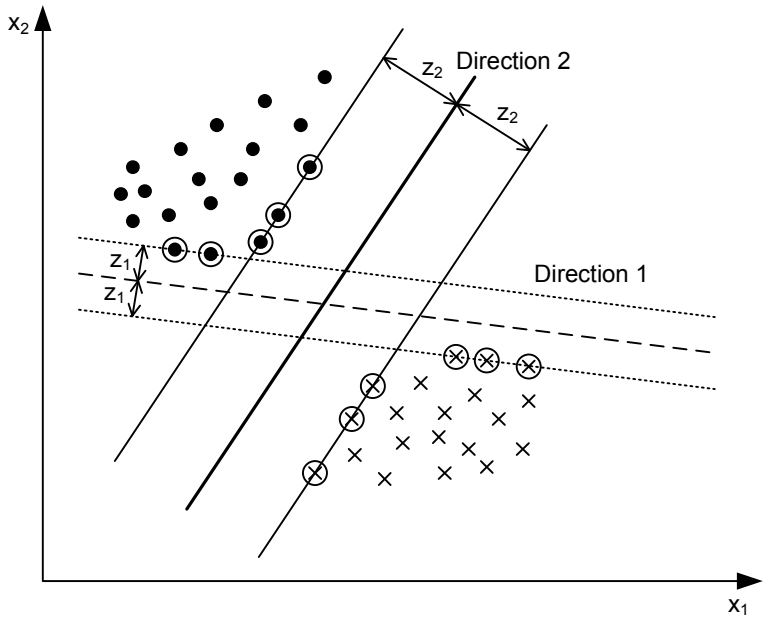

Figure 2.14. Support Vector Machine yields direction 2 of which margin is larger than that of direction 1

Figure 2.14 illustrates an example of a linearly separable two class problem. An encircled data point indicates a support vector, a data point closest to the boundary. With other methods such as the Perceptron Algorithm, direction 1 may be used as the linear decision boundary. However, the SVM guarantees to produce the optimal the linear decision boundary (direction 2) in linearly separable case.

2.2.4.1 Linear Case

The SVM can be used to find linear classifiers. It is mainly different from other linear classifiers in that the hyperplane separating two classes is unique. The linear boundary found using the SVM yields the maximum margin as well.

In general, a hyperplane can be described as

$$g(\mathbf{x}) = \mathbf{w}^T\mathbf{x} + b = 0 \tag{2.59}$$

Using the SVM, a linear classifier for data $\mathbf{X}=\{\mathbf{x}_1,\mathbf{x}_2,\ldots,\mathbf{x}_N\}$ with class labels $\mathbf{t}=\{t_1,t_2,\ldots,t_N\}$, where $t_n\in\{\pm 1\}$, can be built.

The distance between the margin and the hyperplane is equal to $\frac{|g(\mathbf{x})|}{\|\mathbf{w}\|}$ which can be scaled to $\frac{1}{\|\mathbf{w}\|}$. The distance between the two margins is $\frac{2}{\|\mathbf{w}\|}$.

Also,

$$\forall\mathbf{x}\in\omega_1,\ \mathbf{w}^T\mathbf{x}+b\geq 1 \tag{2.60}$$

$$\forall\mathbf{x}\in\omega_2,\ \mathbf{w}^T\mathbf{x}+b\leq -1 \tag{2.61}$$

2.2.4.1.1 Linearly Separable

In linearly separable case, since the maximum margin or the maximum separation between the two classes is required, the hyperplane can be computed so that to

minimize $$J(\mathbf{w})=\frac{1}{2}\|\mathbf{w}\|^2 \tag{2.62}$$

subject to $$t_i(\mathbf{w}^T\mathbf{x}_i+b)\geq 1,\ \text{where}\ \ i=1,2,\ldots,N \tag{2.63}$$

To minimize the above criterion function subject to the constraint, the Lagrangian function

$$L(\mathbf{w},b,\boldsymbol{\lambda})=\frac{1}{2}\mathbf{w}^T\mathbf{w}-\sum_{i=1}^{N}\lambda_i[t_i(\mathbf{w}^T\mathbf{x}_i+b)-1] \tag{2.64}$$

needs to be maximized. λ_i is the Lagrange multiplier. The Karush-Kuhn-Tucker (KKT) conditions must also be satisfied. This yields

$$\mathbf{w}=\sum_{i=1}^{N}\lambda_i t_i\mathbf{x}_i \tag{2.65}$$

$$\sum_{i=1}^{N} \lambda_i t_i = 0 \tag{2.66}$$

$$\boldsymbol{\lambda} \geq \mathbf{0} \tag{2.67}$$

To compute the hyperplane, it is necessary that Lagrange multipliers $\boldsymbol{\lambda}$ are known. These Lagrange multipliers can found by optimizing them using the following equation:

$$\max_{\boldsymbol{\lambda}} \left(\sum_{i=1}^{N} \lambda_i - \frac{1}{2} \sum_{i=1}^{N} \sum_{j=1}^{N} \lambda_i \lambda_j t_i t_j \mathbf{x}_i{}^T \mathbf{x}_j \right) \tag{2.68}$$

subject to $$\sum_{i=1}^{N} \lambda_i t_i = 0 \ , \ \boldsymbol{\lambda} \geq \mathbf{0} \tag{2.69}$$

Then, the hyperplane can be found by substituting the Lagrange multipliers in

$$\mathbf{w} = \sum_{i=1}^{N} \lambda_i t_i \mathbf{x}_i \tag{2.70}$$

$$b = \frac{1}{N_S} \sum_{\mathbf{x}_i \in S} \left(t_i - \mathbf{w}^T \mathbf{x}_i \right) \tag{2.71}$$

where S is the set of support vectors and N_S is the number of support vectors.

2.2.4.1.2 Linearly Non-Separable

In linearly non-separable case, slack variables, ξ_i, are introduced so that

$$t_i (\mathbf{w}^T \mathbf{x}_i + b) \geq 1 - \xi_i \tag{2.72}$$

Each data vector can belong to one of the following three categories:

1) The vector is outside the margin band and correctly classified. ($\xi_i = 0$)

2) The vector is inside the margin band and correctly classified. ($0 < \xi_i \leq 1$)

3) The vector is misclassified. ($\xi_i > 1$)

The criterion function becomes

$$J(\mathbf{w},b,\boldsymbol{\xi}) = \frac{1}{2}\|\mathbf{w}\|^2 + C\sum_{i=1}^{N} I(\xi_i) \tag{2.73}$$

where C is a control parameter, which needs to be minimized subject to

$$t_i(\mathbf{w}^T\mathbf{x}_i + b) \geq 1 - \xi_i \tag{2.74}$$

$$\xi_i \geq 0 \text{ , where } i = 1,2,\ldots,N \tag{2.75}$$

Then, the Lagrangian function becomes

$$\begin{aligned} L(\mathbf{w},b,\boldsymbol{\xi},\boldsymbol{\lambda},\boldsymbol{\mu}) = \frac{1}{2}\|\mathbf{w}\|^2 + C\sum_{i=1}^{N}\xi_i - \sum_{i=1}^{N}\mu_i\xi_i \\ -\sum_{i=1}^{N}\lambda_i[t_i(\mathbf{w}^T\mathbf{x}_i + b) - 1 + \xi_i], \end{aligned} \tag{2.76}$$

where λ_i and μ_i are Lagrange multipliers.

With the KKT conditions, the Lagrange function is maximized subject to

$$\max_{\boldsymbol{\lambda}}\left(\sum_{i=1}^{N}\lambda_i - \frac{1}{2}\sum_{i=1}^{N}\sum_{j=1}^{N}\lambda_i\lambda_j t_i t_j \mathbf{x}_i{}^T\mathbf{x}_j\right) \tag{2.77}$$

$$\sum_{i=1}^{N}\lambda_i y_i = 0 \tag{2.78}$$

$$0 \leq \lambda_i \leq C \text{ , where } i = 1,2,\ldots,N \tag{2.79}$$

Finally, quadratic programming of the Lagrange function subject to the constraints needs to be performed to determine the hyperplane.

2.2.4.2 Non-Linear Case

The SVM for non-linear data is similar to the linear SVM previously explained. The difference is that the non-linear data are mapped into higher dimensional space. That is,

$$\mathbf{x} \in R^l \xrightarrow{K} \mathbf{y} \in R^k \tag{2.80}$$

Then, boundary finding method of the SVM can be performed.

By means of Mercer's Theorem, the Kernel function can be used to perform the mapping. The following are kernel functions used in this study.

Polynomials

$$K(\mathbf{x}, \mathbf{z}) = (\mathbf{x}^T \mathbf{z} + 1)^q \text{ , where } q > 0 \tag{2.81}$$

Radial Basis Functions

$$K(\mathbf{x}, \mathbf{z}) = \exp\left(-\frac{\|\mathbf{x} - \mathbf{z}\|^2}{\sigma^2} \right) \tag{2.82}$$

Hyperbolic Tangent

$$K(\mathbf{x}, \mathbf{z}) = \tanh\left(\beta \mathbf{x}^T \mathbf{z} - \gamma \right) \tag{2.83}$$

$\beta = 2$ and $\gamma = 1$ are recommended for Mercer's conditions (Kernel trick).

To find the Lagrange multipliers of the SVM for a chosen kernel function, we need to perform the following optimization task:

$$\max_{\boldsymbol{\lambda}} \left(\sum_{i=1}^{N} \lambda_i - \frac{1}{2} \sum_{i=1}^{N} \sum_{j=1}^{N} \lambda_i \lambda_j t_i t_j K(\mathbf{x}_i, \mathbf{x}_j) \right) \tag{2.84}$$

subject to $$0 \le \lambda_i \le C \ , \ i = 1, 2, \ldots, N \tag{2.85}$$

$$\sum_{i=1}^{N} \lambda_i t_i = 0 \tag{2.86}$$

The Lagrange multipliers $\lambda_i > 0$ indicates $\mathbf{x}_i$ is a support vector. After the Lagrange multipliers have been obtained, the value of b can be computed by

$$b = \frac{1}{N_S} \sum_{\mathbf{x}_i \in S} \left(t_i - \sum_{\mathbf{x}_j \in S} \lambda_j t_j K(\mathbf{x}_i, \mathbf{x}_j) \right) \tag{2.87}$$

where S is the set of support vectors and N_S is the number of support vectors.

The resulting classifier then becomes

$$g(\mathbf{x}) = \sum_{\mathbf{x}_i \in S} \lambda_i t_i K(\mathbf{x}, \mathbf{x}_i) + b \tag{2.88}$$

$$\mathbf{x} \in \begin{cases} \omega_1, g(\mathbf{x}) > 0 \\ \omega_2, g(\mathbf{x}) < 0 \end{cases} \tag{2.89}$$

2.2.5 Clustering

In addition to the proposed method, Fuzzy C-Mean (FCM) and Hard C-Mean (HCM) clustering techniques were applied to the data to verify whether the healthy and defective bearing data could be easily grouped.

Clustering is an unsupervised machine learning method to classify unknown data into different groups so that the data in each group shares common characteristics. Clustering starts with a number of clusters, each with a prototype or centroid. During each iteration, the distance of all vectors to each prototype is computed. Then, the prototypes are updated. This is repeated until the convergence condition is met.

The general theory of FCM and HCM is presented in the next subsections. The underlying detail of the clustering is not presented since one can find it in most pattern recognition textbooks.

2.2.5.1 Fuzzy C-Mean Clustering

To cluster $X = \{\vec{x}_1, \ldots, \vec{x}_N\}$ into c clusters $\{A_i\}_{i=i}^{c}$, we have prototypes

$$V = \{\vec{v}_1, \ldots, \vec{v}_c\}, \tag{2.90}$$

partition matrix

$$U_{c \times N} = (u_{ik}), \tag{2.91}$$

where u_{ik} is the membership of $\vec{x}_k$ in A_i,

the criterion function

$$J_q(U,V) = \sum_{k=1}^{N} \sum_{i=1}^{c} (u_{ik})^q \cdot d(\vec{x}_k, \vec{v}_i), \tag{2.92}$$

where $d(\vec{x}_k, \vec{v}_i)$ is a distance measure and q is the fuzzifier,

and a constraint

$$\sum_{i=1}^{c} u_{ik} = 1 \tag{2.93}$$

where $u_{ik} \in [0,1]$.

Minimizing $J_q(U,V)$ with the constraint, we have

$$u_{ik} = \frac{\left(\frac{1}{d(\vec{x}_k, \vec{v}_i)}\right)^{\frac{1}{q-1}}}{\sum_{j=1}^{c} \left(\frac{1}{d(\vec{x}_k, \vec{v}_j)}\right)^{\frac{1}{q-1}}} \tag{2.94}$$

and

$$\vec{v}_i = \frac{\sum_{k=1}^{N} (u_{ik})^q \cdot \vec{x}_k}{\sum_{k=1}^{N} (u_{ik})^q} \tag{2.95}$$

FCM Algorithm can be summarized as follows:

1: Fix *c*.
2: Pick a distance measure $d(\vec{x}_k, \vec{v}_i)$.
3: Pick $q > 1$ and $\varepsilon > 0$.
4: Set $t = 0$.
5: Initialize $V^{(0)} = \{\vec{v}_1^{(0)}, \ldots, \vec{v}_c^{(0)}\}$.
6: Do
7: Compute $U^{(t)} = \{u_{ik}\}_{i=1,k=1}^{c \quad N}$
8: Increment *t*.
9: Recompute $V^{(t)} = \{\vec{v}_i\}_{i=1}^{c}$
10: Until convergence based on ε.

2.2.5.2 Hard C-Mean Clustering

Hard C-Means clustering is a restricted version of FCM with $u_{ik} = \{0,1\}$ and $q = 1$. The algorithm is adapted from what is given in class in order to eliminate the calculation of *V* problem in the first iteration, i.e. if $\sum_{k=1}^{N} u_{ik}{}^{(l-1)}$ for cluster A_i is equal to zero, then $\vec{v}_i$ will always be $\vec{0}$ forever.

HCM Algorithm can be summarized as follows:

1: Fix *c*.
2: Pick a distance measure $d(\vec{x}_k, \vec{v}_i)$.
3: Pick $\varepsilon > 0$.
4: Set $l = 1$.
5: Initialize $V^{(0)} = \{\vec{v}_1^{(0)}, \ldots, \vec{v}_c^{(0)}\}$.
6: Do
7: For *i* = 1 to *c*
8: For *k* = 1 to *N*
9: Compute $u_{ik}{}^{(l)} = \begin{cases} 1, & i = \arg\min_j \left\{ d(\vec{x}_k, \vec{v}_j)^{(l)} \right\} \\ 0, & \text{otherwise} \end{cases}$
10: End For

11: End For

12: For $i = 1$ to c

13: Recompute $\vec{v}_i^{(l)} = \dfrac{\sum_{k=1}^{N} u_{ik}^{(l-1)} \cdot \vec{x}_k}{\sum_{k=1}^{N} u_{ik}^{(l-1)}}$

14: End For

15: Until convergence based on ε.

2.2.5.3 Distance Measure

The only distance measure experimented was the Euclidean distance, which is defined as in Equation 2.96.

Euclidean Distance

$$d_e^2(\vec{x}, \vec{y}) = (\vec{x} - \vec{y})^T (\vec{x} - \vec{y}) \tag{2.96}$$

This chapter describes the background information on ASD's, the characteristic of bearing faults, and theoretical background of the techniques used. Having been described, these techniques are incorporated into the proposed method in the next chapter. The algorithm of the implementation of signal processing, wavelet packet decomposition, the support vector machine, and the genetic algorithm are discussed. In addition, it includes the information of the hardware setup

CHAPTER 3 IMPLEMENTATION OF ALGORITHM

In this study, stator current data from the ASD system are collected from both healthy and defective bearings for an ASD system fundamental frequency and defect type. Several process steps are then applied to the data to detect ball bearing defects. The detailed implementation of the bearing fault detection for ASD systems is discussed in this chapter. The method combines various techniques, including the wavelet packet transform, the genetic algorithm, and the support vector machine. In addition, details of the hardware system, its setup, and data acquisition are also provided.

3.1 Procedures

To generate an SVM classifier, the captured stator current data must undergo several processes. First, the fundamental frequency of the current samples is suppressed. Then, the resulting signal is decomposed into wavelet packet nodes, where each node corresponds to a frequency band and contains wavelet packet coefficients (WPC's). The RMS value of each node can be computed from the WPC's. Only nodes into which the characteristic frequencies and modulated characteristic frequencies fall are used in the next step. In this method, the GA is used for the feature (or node) selection to be used in the SVM. The GA selects initial chromosomes (or sets) of nodes of interest and, then, computes the fitness of each chromosome, or the SVM classification error, and then recombines the chromosomes to produce the next-generation chromosomes of nodes. The process is repeated until convergence is reached. In the end, the GA-generated

chromosome of WP nodes which yields the best SVM classifier is chosen and the SVM classifier is determined. Figure 3.1 shows the overview of the proposed method. Figure 3.1 depicts the steps of the algorithm presented in this study.

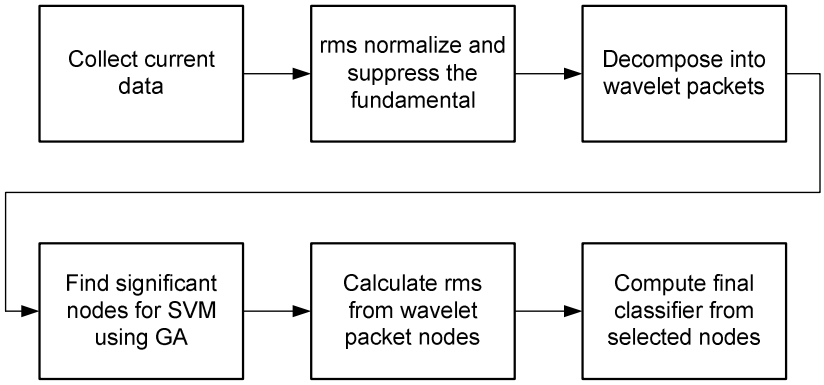

Figure 3.1. Steps of the proposed algorithm

3.1.1 Current Sampling

The data acquisition is accomplished by using an industrial circuit monitor, namely the SquareD CM4000 series Circuit Monitor. It is capable of sampling 3-phase voltages and currents, or 8 channels, at up to 30,720 Hz per channel. The Circuit Monitor is equipped with an onboard non-volatile memory for storing captured waveform data. The data on the non-volatile memory can be uploaded to the PC via either the serial or Ethernet connection. Since the carrier frequency of the PWM inverter is fixed at 9.2 kHz, the stator current data is sampled at the maximum sampling capability of the circuit monitor to avoid aliasing. The length of the current data to be sampled is determined by the number of levels of wavelet packet decomposition. In this study, the stator current data of the ASD motor is sampled at 30,720 points per second for 3 seconds, or 92,160 samples in total, by the SquareD CM4000 Circuit Monitor.

3.1.2 Signal Preprocessing

Each captured ASD current waveform is preprocessed before it is decomposed into wavelet packets. First, the current data is normalized by its rms value.

$$x_{rms} = \sqrt{\frac{1}{N}\sum_{n} x^2(n)} \ , \tag{3.1}$$

where $n = 0, \ldots, N-1$

$$x'(n) = \frac{x(n)}{x_{rms}} \tag{3.2}$$

Because the sampled current waveform contains a significant system fundamental component, it needs to be suppressed. The characteristic frequency fault harmonics induced by bearing faults are used to differentiate the good and defective bearings. However, the magnitude of the bearing fault induced frequency components is relatively much smaller than that of the system fundamental and is likely to be overwhelmed. As a result, the system fundamental must be suppressed to reduce its significance before the signal is decomposed into wavelet packets.

A second-order notch filter is used for system fundamental suppression. The transfer function of the notch filter is given by

$$H(z^{-1}) = \frac{A(\beta z^{-1})}{A(\alpha z^{-1})} = \frac{1 + \beta a z^{-1} + \beta^2 z^{-2}}{1 + \alpha a z^{-1} + \alpha^2 z^{-2}} \tag{3.3}$$

where

$$0 \le \alpha < 1, \quad 0 \le \beta \le 1 \tag{3.4}$$

and

$$a = -2\cos(\omega) \text{ for } -\pi \le \omega \le \pi \tag{3.5}$$

The parameter a corresponds to the frequency to suppress. The values of α and β reflect the poles and zeros, respectively, which control the filter gain and bandwidth.

The system frequency to be suppressed is determined by the FFT. The highest peak of the spectrum indicates the system fundamental. The frequency value is then substituted in Equation (3.3)

3.1.3 Wavelet Packet Decomposition

The data samples are to be wavelet packet decomposed into 7.5 Hz frequency bands. With the sampling frequency of 30.72 kHz, this requires 11 levels of WPD. The preprocessed current waveform data is decomposed into 7.5 Hz wavelet packets. Since the number of samples must be a power of 2, only 2^{16}, or 65,536, points of the notch filtered data are used. For the waveform data sampled at 30,720 Hz, the decomposition is performed with 11-level wavelet packet decomposition. There are 2,048 (or 2^{11}) resulting wavelet packets (or nodes) and each wavelet packet contains 32 coefficients, which are used to compute its rms value to represents the 7.5 Hz frequency band.

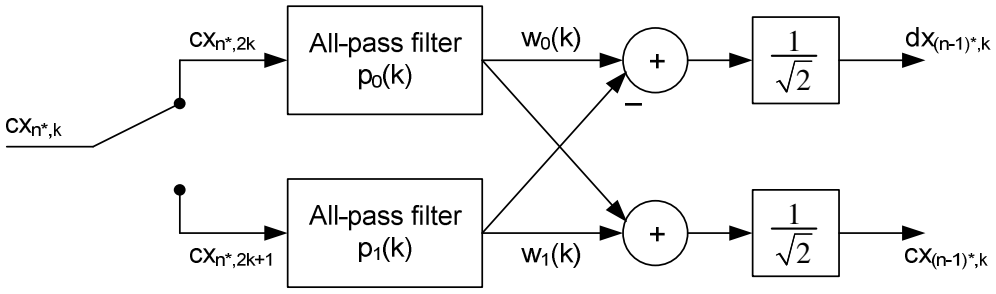

Figure 3.2. Elliptic IIR half-band filter composed of all-pass filters

The wavelet packet filter used in the study is using a special all-pass implementation of elliptic half-band IIR (L=3) filters. The filter offers good frequency separation between adjacent bands and low computational complexity [6].

3.1.4 rms Calculations of Characteristic Frequency Bands

The result from the wavelet packet decomposition is the wavelet packet coefficients. The coefficients of each wavelet packet frequency band represent the time localization of its respective frequency range. The rms value of node (j, p) can be computed using the wavelet packet coefficients, $d_{j,k}^{p}$, by

$$x_{rms}(j,p) = \sqrt{\frac{1}{K}\sum_{k}(d_{j,k}^{p})^{2}} \tag{3.6}$$

where

$$d_{j+1,k}^{2p} = d_{j,k}^{p} * \bar{h}(2k) \tag{3.7}$$

and

$$d_{j+1,k}^{2p+1} = d_{j,k}^{p} * \bar{g}(2k) \tag{3.8}$$

3.1.5 Wavelet Packet Node Selection using Genetic Algorithm

Since the magnitudes of the fault induced frequency components are very small and the ASD current contains high random EMI noise resulting from the PWM input voltage waveform, the noise magnitudes at some frequencies are high and overshadow the magnitudes of the fault harmonics. This would reduce the significance of the frequency bands of interest and reduce the ability to detect bearing faults. Therefore, only frequency bands least affected by the EMI noise should be used in classification.

Recalling Equation (2.27),

$$f_{CF,ASD} = \left| n f_f \pm m f_v \right| \tag{3.9}$$

where

f_f = fundamental supply frequency in Hertz
f_v = vibration frequency in Hertz
n = PWM harmonic index of fundamental supply
m = vibration modulation index

Significant wavelet packet nodes are selected by the genetic algorithm. The wavelet packet nodes of interest for a system fundamental and a bearing fault type can be determined from the frequencies of interest (Equation 3.9). The rms values of these wavelet packet nodes in an ASD system with bearing defects would be measurably larger than those in a system with no defects. However, the ASD current contains high random EMI noise, which diminishes the significance of fault induced frequency components. Using only frequency bands least affected by the EMI noise in the classification is highly preferable.

To select significant wavelet packet nodes, the genetic algorithm is used. Each chromosome in this study consists of a binary string. Each binary value, or gene, in the string represents a wavelet packet node of interest. If the value of a gene is 1, then, the corresponding wavelet packet node is used in classification. Otherwise, the node is not.

The fitness of each chromosome can be evaluated using the SVM. The rms values of the wavelet packet nodes are selected according to the chromosomes. An SVM classifier can be determined from a set of good and defective bearing data. A ten-fold

classification error can be computed. This classification error reveals how well the set of wavelet packet nodes can produce an SVM classifier.

In each generation, the chromosomes reproduce offspring by recombination and mutation and some of the elites are kept. The reproduction strategy applied in the study is two-point crossover and section mutation. Some of the top chromosomes or elites, chromosomes with highest fitness, are kept in the next-generation population as well.

In this study, the convergence condition is when the best chromosome has not changed for a number of generations or when the number of generations exceeds the limit. When the GA converges, the resulting chromosome yields a set of wavelet packet nodes that produces the least percent error for the bearing fault condition at the system frequency. These nodes contain pronounced fault induced frequency components and are supposedly least affected by the EMI noise.

3.1.6 Decision Boundary Finding with Support Vector Machine

For each bearing fault type and each ASD system fundamental, the rms values of the wavelet packet nodes corresponding to bearing fault characteristic frequencies selected by the GA are used as features in the SVM classification. A class label vector is created. Each entry in this vector corresponds to a WP node rms vector from either the healthy or defective bearing. If a WP node rms vector is from the healthy bearing, it is labeled as 1 in the class label vector. Otherwise, it is labeled as -1. With a set of WP node rms vectors and the class label vector and a given kernel, the SVM produces a classifier.

In this study, a ten-fold classification error is computed. That is, the WP node rms vectors are divided into 2 groups. In the first group, ninety percent of the vectors are

used in classifier calculation; in the other group, the other ten percent is used to evaluate the resulting classifier. This is performed 10 times. In each time, the groups contain different vectors. The fitness is the average percent error of the ten-fold classification error. Figure 3.3 illustrates the steps to determine the 10-fold classification error.

Ultimately, after the GA converges, the final set of WP nodes is determined. The final SVM classifier can be computed using all the vectors for the bearing fault type and the ASD system frequency.

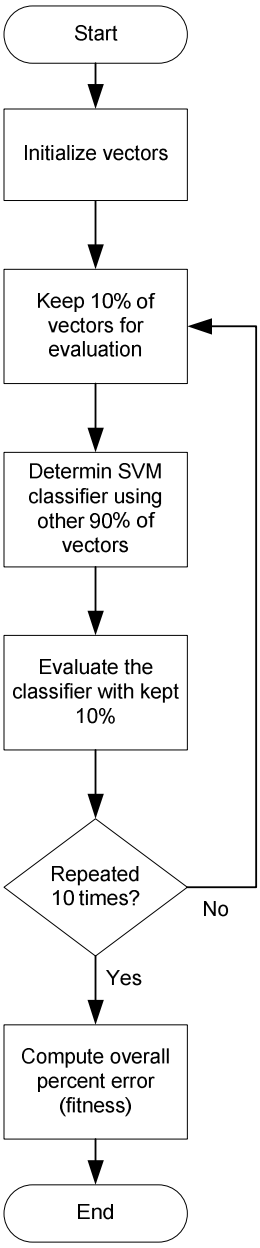

Figure 3.3. Steps to determine the ten-fold classification error

3.2 Hardware Setup

The test ASD test system consists of an inverter capable of outputting PWM voltage waveforms with fundamental frequencies from 0.1 to 400 Hz and a carrier frequency of 9.2 kHz and a 1-hp, 3450 rpm, 208-volt, 60-Hz, 3-phase, 2-pole induction motor. Due to the specifications of the motor, the maximum output frequency of the inverter is limited to 60 Hz to prevent any damages. Both end bearings are 6203-ZZ-C3 (8 balls). Outer race and cage defects on the shaft end ball bearing were tested against a healthy bearing. For each defect case, the PWM outputs from the inverter at 15, 30, 45, and 60 Hz are used, which produce no load speeds of 897.6, 1797, 2697, and 3596 rpm, respectively. The current data is sampled at 30,720 Hz for 3 seconds.

The outer race defect was tested with a belt driven load to provide a radial load on the bearing. In the tests a single 1.59 mm (1/16 inch) diameter hole was drilled on the outer race to simulate an outer race defect. Table 3.1 shows the vibration frequencies of the outer race defect when the ASD system runs at different fundamental frequencies.

System freq. (Hz)	Rotor speed (rpm)	f_{OD} (Hz)
15	897.6	47.9
30	1797	95.8
45	2697	143.8
60	3596	191.8

Table 3.1. Outer race defect vibration frequencies at different ASD system frequencies

Table 3.2 shows characteristic frequencies resulting from the modulation of PWM fundamental and the outer race defect vibration frequency as described by Equation 3.5. Here only the first thirty frequencies are listed. The corresponding wavelet packet node number into which each frequency falls is also shown. It is important to note that some adjacent characteristic frequencies are in the same frequency band and, thus, have the

same WP node number. The rms values of these WP nodes are used to create an SVM classifier.

Motor Input Fundamental Frequency							
15 Hz		30 Hz		45 Hz		60 Hz	
Fault Harmonic Freq. (Hz)	WP Node No	Fault Harmonic Freq. (Hz)	WP Node No	Fault Harmonic Freq. (Hz)	WP Node No	Fault Harmonic Freq. (Hz)	WP Node No
2.9	1	5.8	1	8.8	2	11.8	2
8.6	2	17.5	3	26.5	4	35.4	5
9.3	2	18.3	3	27.3	4	36.4	5
15.0	3	30.0	5	45.0	7	60.0	9
20.7	3	41.7	6	62.7	9	83.6	12
21.4	3	42.5	6	63.5	9	84.6	12
27.1	4	54.2	8	81.2	11	108.2	15
32.9	5	65.8	9	98.8	14	131.8	18
38.6	6	77.5	11	116.5	16	155.4	21
39.3	6	78.3	11	117.3	16	156.4	21
45.0	7	90.0	13	135.0	19	180.0	25
50.7	7	101.7	14	152.7	21	203.6	28
51.4	7	102.5	14	153.5	21	204.6	28
57.1	8	114.2	16	171.2	23	228.2	31
62.9	9	125.8	17	188.8	26	251.8	34
68.6	10	137.5	19	206.5	28	275.4	37
69.3	10	138.3	19	207.3	28	276.4	37
75.0	11	150.0	21	225.0	31	300.0	41
80.7	11	161.7	22	242.7	33	323.6	44
81.4	11	162.5	22	243.5	33	324.6	44
87.1	12	174.2	24	261.2	35	348.2	47
92.9	13	185.8	25	278.8	38	371.8	50
98.6	14	197.5	27	296.5	40	395.4	53
99.3	14	198.3	27	297.3	40	396.4	53
105.0	15	210.0	29	315.0	43	420.0	57
110.7	15	221.7	30	332.7	45	443.6	60
111.4	15	222.5	30	333.5	45	444.6	60
117.1	16	234.2	32	351.2	47	468.2	63
122.9	17	245.8	33	368.8	50	491.8	66
128.6	18	257.5	35	386.5	52	515.4	69
129.3	18	258.3	35	387.3	52	516.4	69
135.0	19	270.0	37	405.0	55	540.0	73
140.7	19	281.7	38	422.7	57	563.6	76
141.4	19	282.5	38	423.5	57	564.6	76
147.1	20	294.2	40	441.2	59	588.2	79
152.9	21	305.8	41	458.8	62	611.8	82
158.6	22	317.5	43	476.5	64	635.4	85
159.3	22	318.3	43	477.3	64	636.4	85

Table 3.2. Outer Race Defect Harmonic Frequencies

In the bearing cage defect case, the bearing cage was deformed between two adjacent balls with a center punch to interfere with normal cage rotation. The bearing cage defect mechanical frequencies are show in Table 3.3.

System freq. (Hz)	Rotor speed (rpm)	f_{CD} (Hz)
15	897.6	5.98
30	1797	12.0
45	2697	18.0
60	3596	24.0

Table 3.3. Cage defect vibration frequencies at different ASD system frequencies

Similarly, Table 3.4 lists the characteristic frequencies produced by means of modulation between the PWM input voltage and cage defect vibration and their corresponding WP nodes.

Motor Input Fundamental Frequency							
15 Hz		30 Hz		45 Hz		60 Hz	
Fault Harmonic Freq. (Hz)	WP Node No	Fault Harmonic Freq. (Hz)	WP Node No	Fault Harmonic Freq. (Hz)	WP Node No	Fault Harmonic Freq. (Hz)	WP Node No
3.0	1	5.9	1	8.9	2	11.9	2
3.0	1	6.0	1	9.0	2	12.1	2
9.0	2	18.0	3	27.0	4	36.0	5
15.0	3	30.0	5	45.0	7	60.0	9
21.0	3	42.0	6	63.0	9	84.0	12
27.0	4	54.0	8	81.0	11	108.0	15
27.1	4	54.1	8	81.1	11	108.1	15
33.0	5	65.9	9	98.9	14	131.9	18
33.0	5	66.0	9	99.0	14	132.1	18
39.0	6	78.0	11	117.0	16	156.0	21
45.0	7	90.0	13	135.0	19	180.0	25
51.0	7	102.0	14	153.0	21	204.0	28
57.0	8	114.0	16	171.0	23	228.0	31
57.1	8	114.1	16	171.1	23	228.1	31
63.0	9	125.9	17	188.9	26	251.9	34
63.0	9	126.0	17	189.0	26	252.1	34
69.0	10	138.0	19	207.0	28	276.0	37
75.0	11	150.0	21	225.0	31	300.0	41
81.0	11	162.0	22	243.0	33	324.0	44
87.0	12	174.0	24	261.0	35	348.0	47
87.1	12	174.1	24	261.1	35	348.1	47
93.0	13	185.9	25	278.9	38	371.9	50
93.0	13	186.0	25	279.0	38	372.1	50
99.0	14	198.0	27	297.0	40	396.0	53
105.0	15	210.0	29	315.0	43	420.0	57
111.0	15	222.0	30	333.0	45	444.0	60
117.0	16	234.0	32	351.0	47	468.0	63
117.1	16	234.1	32	351.1	47	468.1	63
123.0	17	245.9	33	368.9	50	491.9	66
123.0	17	246.0	33	369.0	50	492.1	66
129.0	18	258.0	35	387.0	52	516.0	69
135.0	19	270.0	37	405.0	55	540.0	73
141.0	19	282.0	38	423.0	57	564.0	76
147.0	20	294.0	40	441.0	59	588.0	79
147.1	20	294.1	40	441.1	59	588.1	79
153.0	21	305.9	41	458.9	62	611.9	82
153.0	21	306.0	41	459.0	62	612.1	82
159.0	22	318.0	43	477.0	64	636.0	85
165.0	23	330.0	45	495.0	67	660.0	89
171.0	23	342.0	46	513.0	69	684.0	92

Table 3.4. Cage Defect Harmonic Frequencies

In this chapter, the steps of the proposed algorithm have been discussed. In the next chapter, the results of the algorithm from both clustering and the proposed method are provided. The ASD current waveforms at different fundamental frequencies before and after wavelet packet decomposition are presented. The percent errors of clustering and the proposed method are presented as well as the WP nodes selected by the algorithm.

CHAPTER 4 RESULTS OF IMPLEMENTATION

The ASD test system was set up according to Section 3.2. The ASD current data waveforms were captured using the SquareD circuit monitor at 30,720 Hz for 3 seconds as mentioned in the previous chapter. A total of xx data captures were performed as follows: Four ASD system fundamental frequencies, 15, 30, 45, and 60 Hz, were measured for each type of bearing condition. Three types of bearing conditions—healthy, cage defect, and outer race defect—were monitored. In the bearing cage defect case, the bearing cage was deformed between two adjacent balls with a center punch to interfere with normal cage rotation. In the bearing outer race defect, a single 1.59 mm (1/16 inch) diameter hole was drilled on the outer race to simulate an outer race defect. In this chapter, illustrations of the captured current data and the results from clustering and the proposed method are presented. The results from clustering are to be compared with the results from the proposed method.

The characteristic frequencies of each bearing condition at each fundamental can be computed using Equation 3.9. The speed of the ASD at no load with the fundamental at 15, 30, 45, and 60 Hz was 897.6, 1,797, 2,697, and 3,596 RPM or 14.96, 29.95, 44.95, and 59.93 revolutions per second, respectively.

The time domain plots of samples of ASD current waveform data at system fundamental frequencies of 15, 30, 45, and 60 Hz are displayed in Figure 4.1. Noise resulting from the PWM inverter switching and EMI appear in large quantity in all fundamentals.

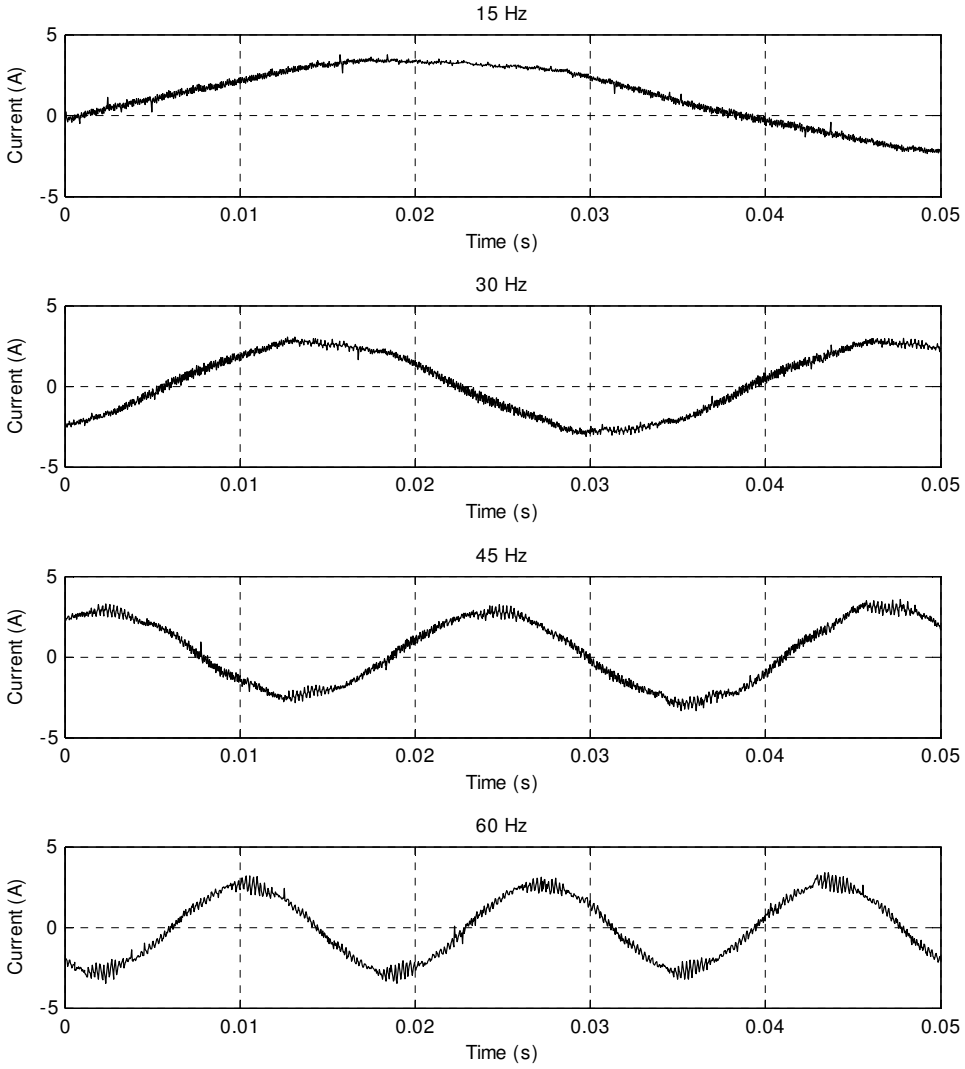

Figure 4.1. ASD current data with the system fundamental of 15, 30, 45, and 60 Hz

Each captured current waveform was normalized by its rms value and the fundamental frequency component in the waveform was removed using the aforementioned notch filter. The spectrum of the current waveforms after rms normalization and fundamental removal can be computed using the FFT. Figures 4.2-4.5

illustrate the FFT of rms-normalized current data of the ASD system with healthy, cage defect, and outer race defect bearings at system fundamental of 15, 30, 45, and 60 Hz.

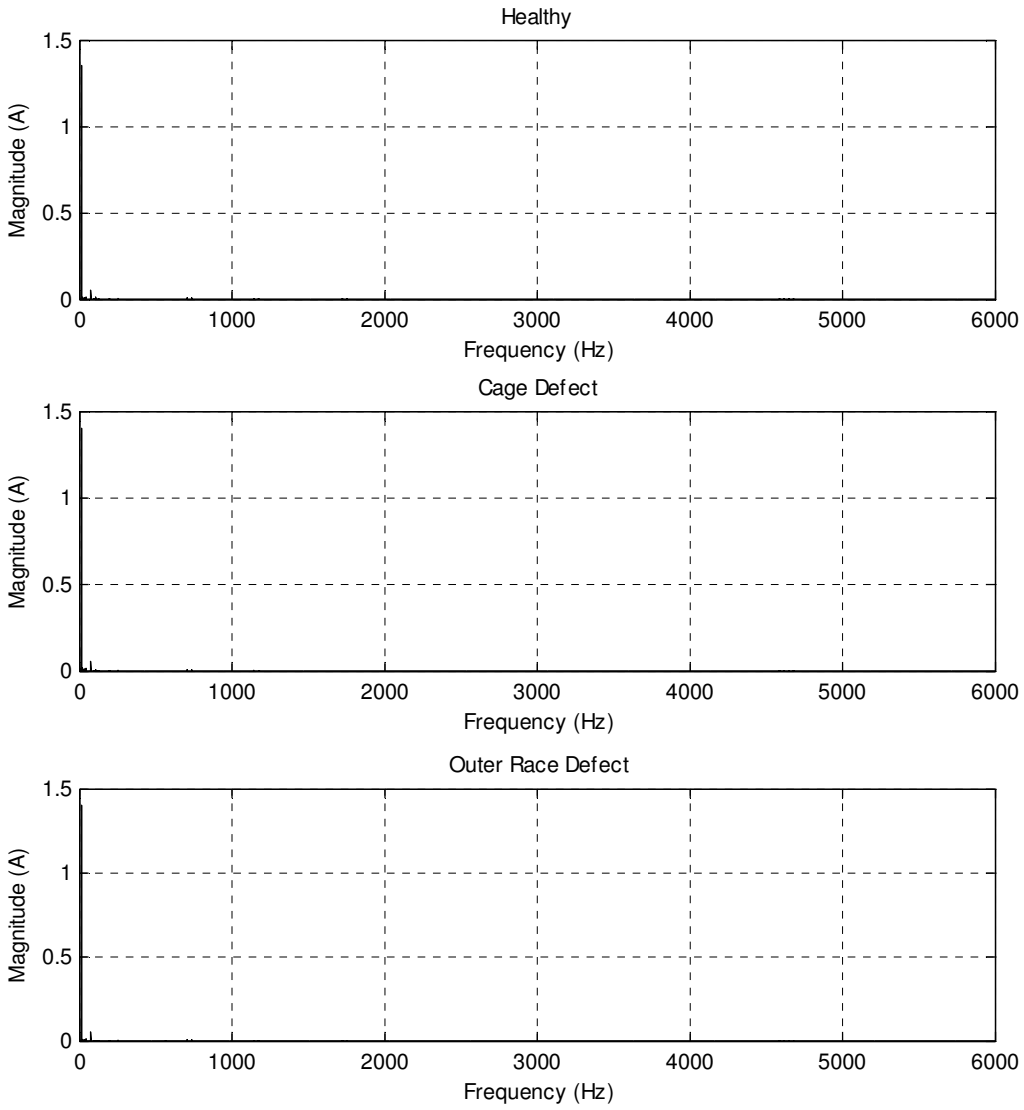

Figure 4.2. FFT of the rms-normalized ASD current data at 15 Hz with (a) healthy, (b) cage defect, and (c) outer race defect bearings

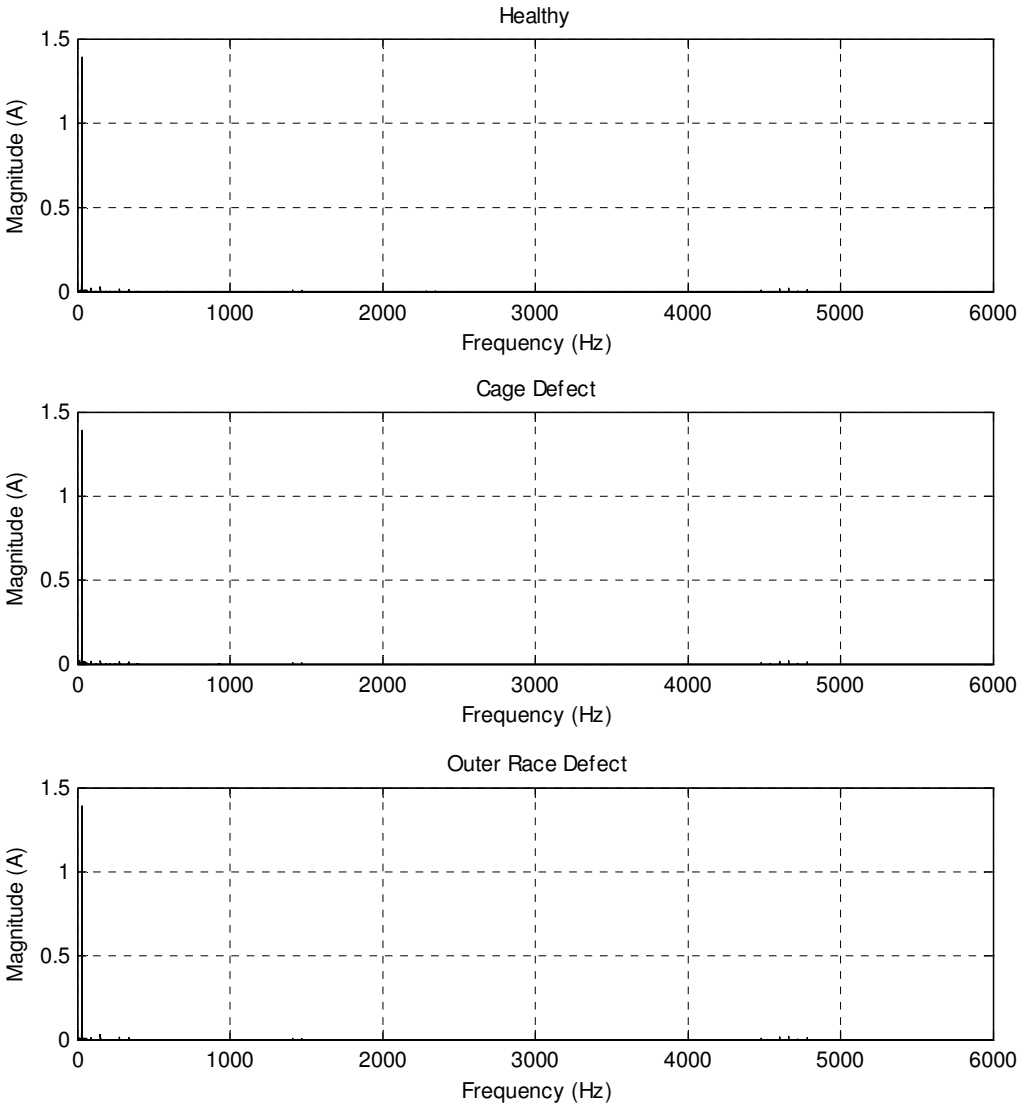

Figure 4.3. FFT of the rms-normalized ASD current data at 30 Hz with (a) healthy, (b) cage defect, and (c) outer race defect bearings

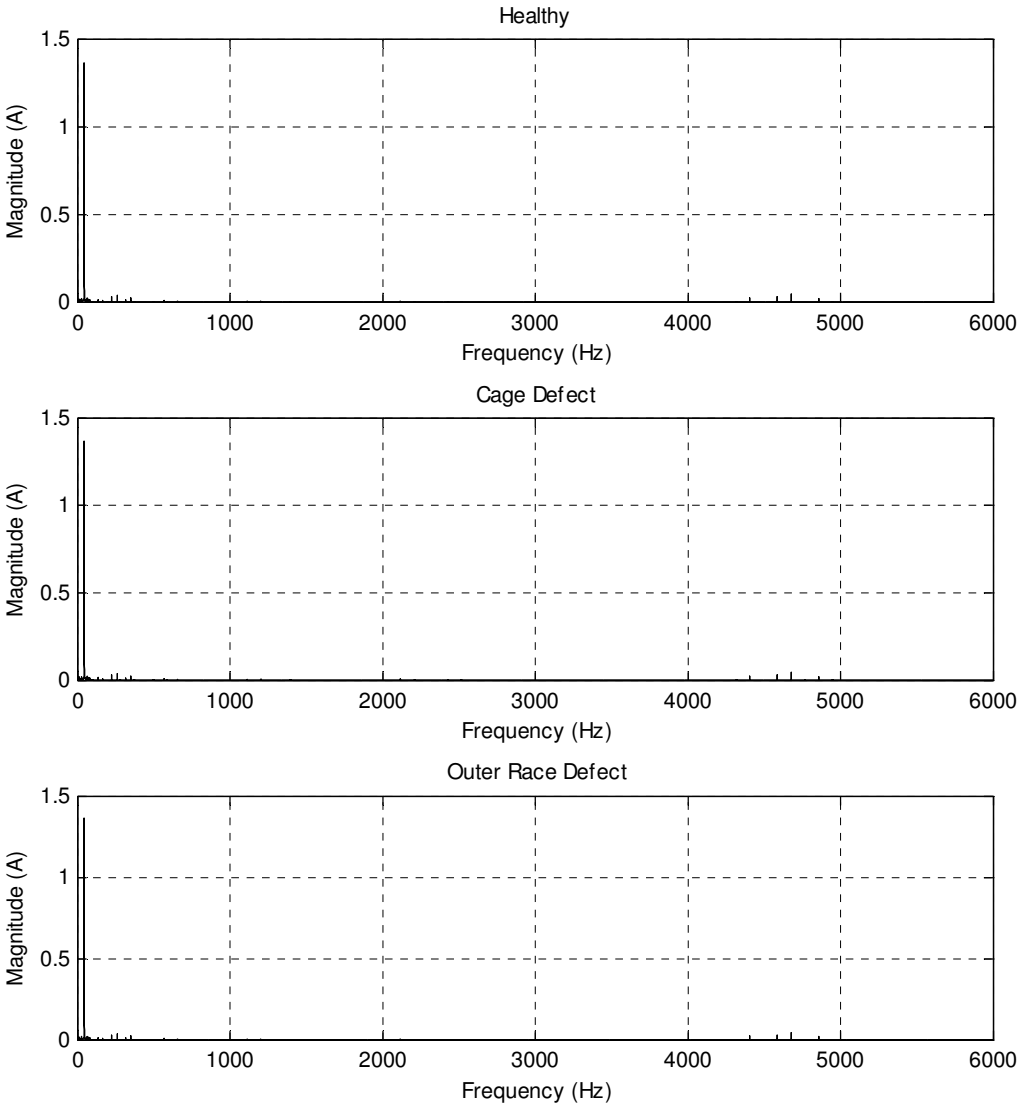

Figure 4.4. FFT of the rms-normalized ASD current data at 45 Hz with (a) healthy, (b) cage defect, and (c) outer race defect bearings

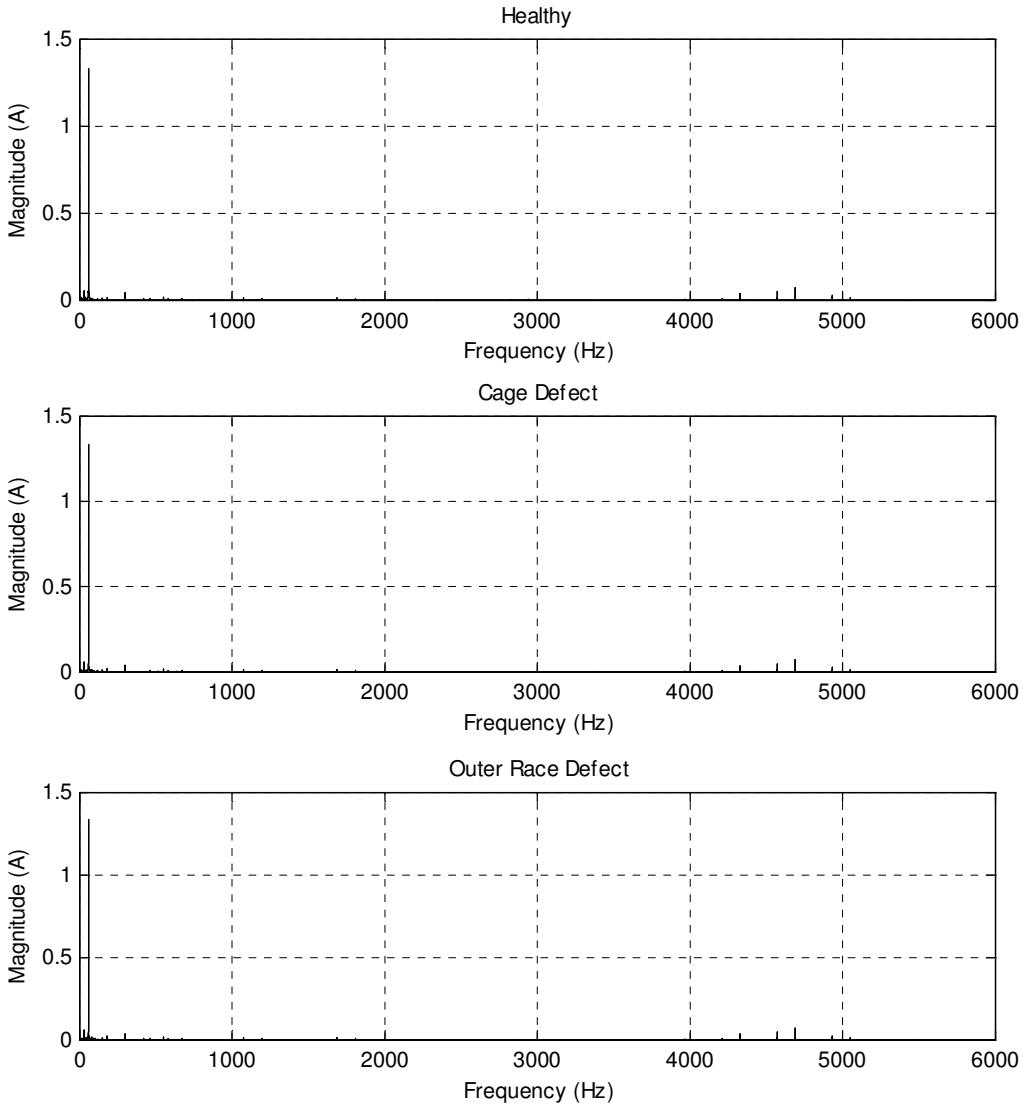

Figure 4.5. FFT of the rms-normalized ASD current data at 60 Hz with (a) healthy, (b) cage defect, and (c) outer race defect bearings

Figures 4.6-4.9 illustrate the FFT of rms-normalized fundamental-removed current data of the ASD system with healthy, cage defect, and outer race defect bearings at system fundamental of 15, 30, 45, and 60 Hz.

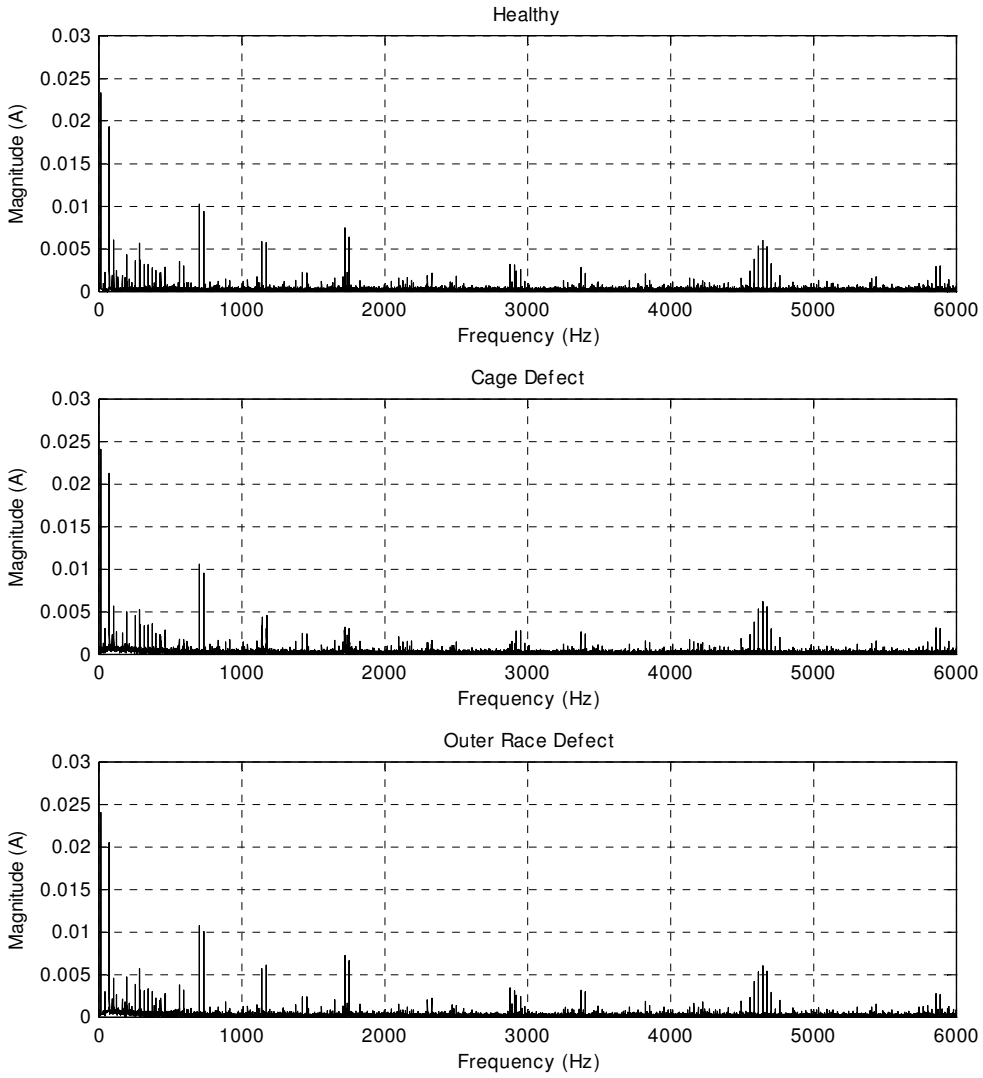

Figure 4.6. FFT of the rms-normalized fundamental-removed ASD current data at 15 Hz with (a) healthy, (b) cage defect, and (c) outer race defectbearings

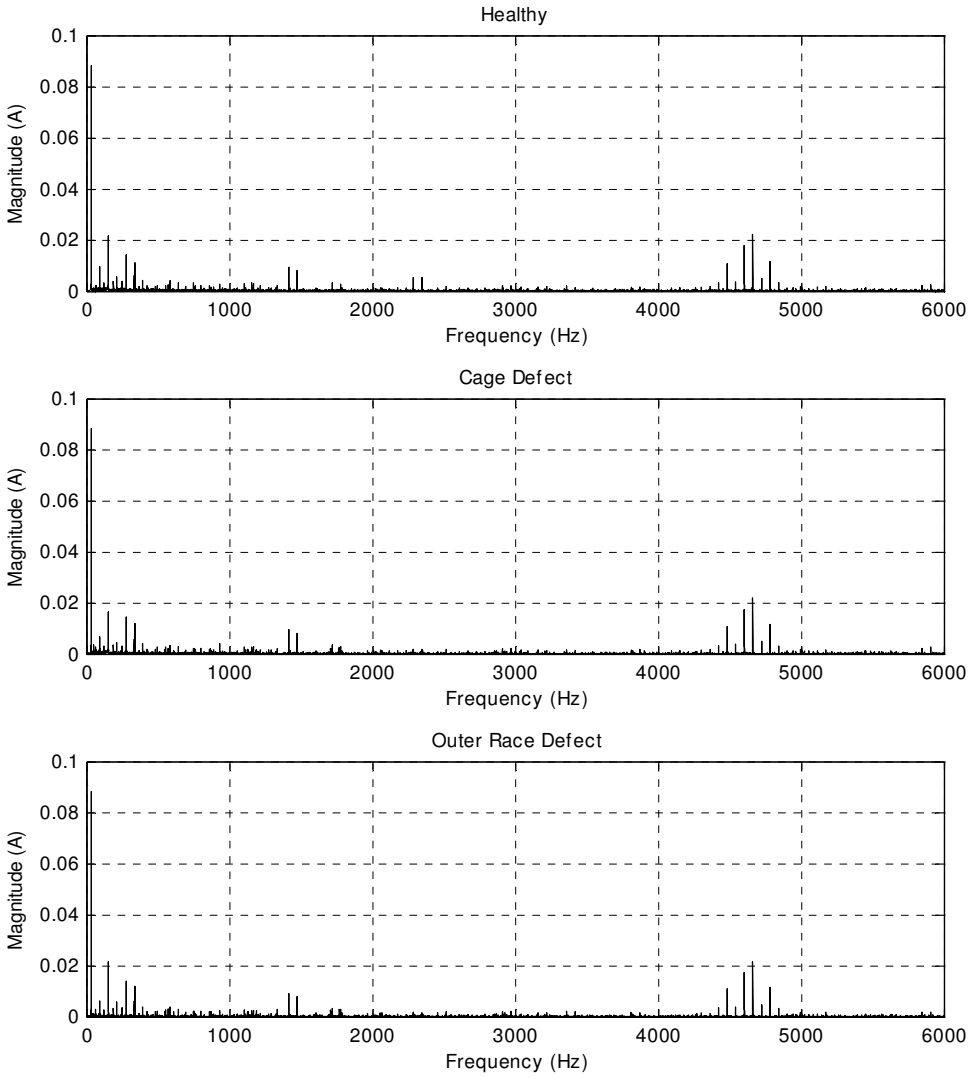

Figure 4.7. FFT of the rms-normalized fundamental-removed ASD current data at 30 Hz with (a) healthy, (b) cage defect, and (c) outer race defect bearings

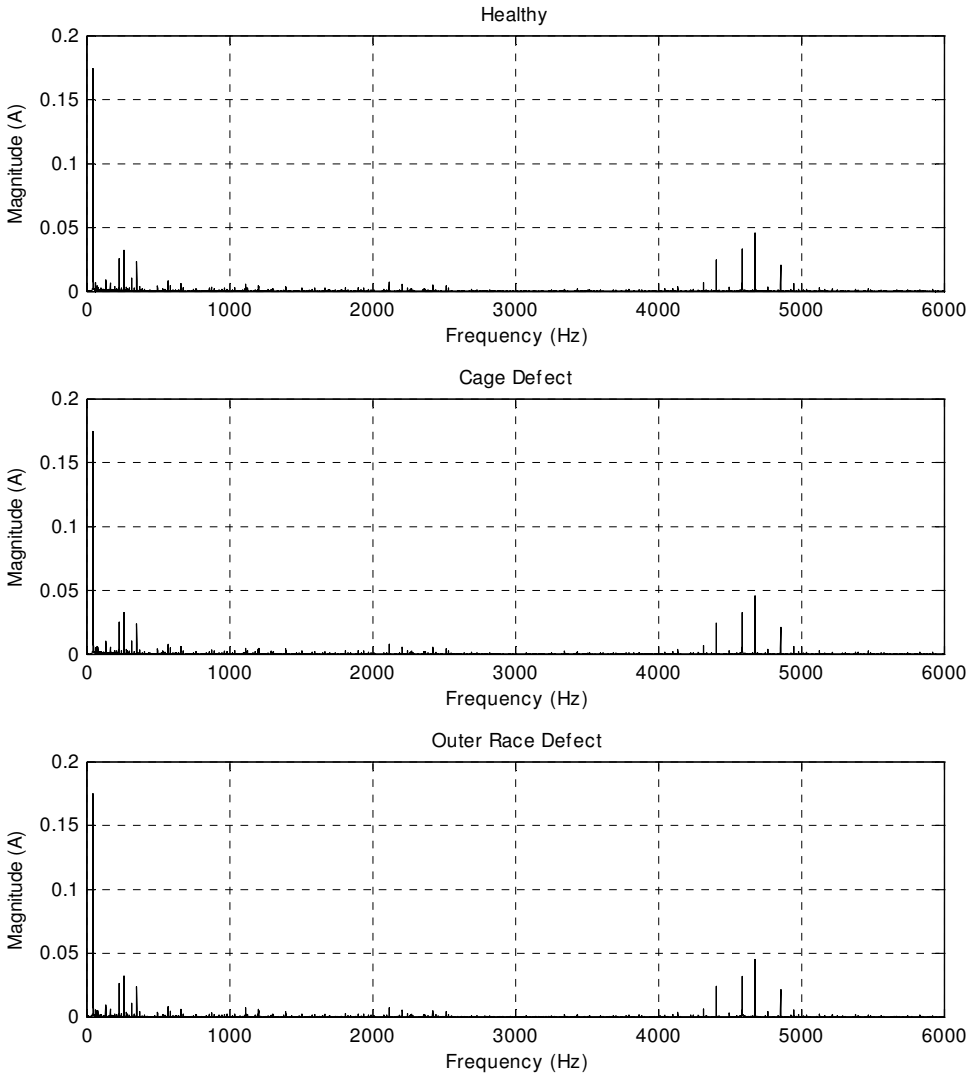

Figure 4.8. FFT of the rms-normalized fundamental-removed ASD current data at 45 Hz with (a) healthy, (b) cage defect, and (c) outer race defect bearings

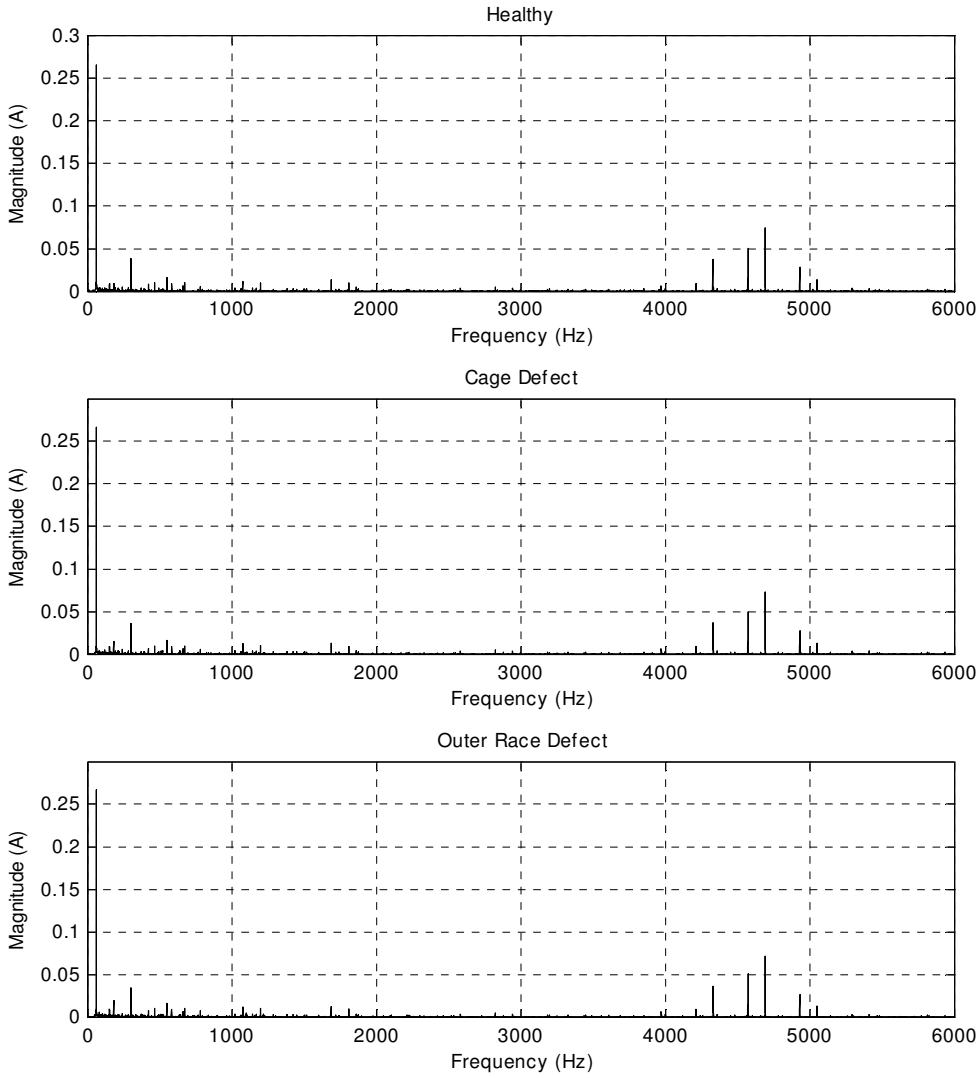

Figure 4.9. FFT of the rms-normalized fundamental-removed ASD current data at 60 Hz with (a) healthy, (b) cage defect, and (c) outer race defect bearings

From the FFT plots above, one can see, even though it was already notch filtered, the fundamental components still retained its dominance though it was suppressed by some 2.662, 6.353, 12.79, and 19.98 % respectively for the 15, 30, 45, and 60 Hz fundamentals.

Eleven-level wavelet packet decomposition was applied to the rms-normalized fundamental-removed ASD current data. There were 92,160 data points per capture. After rms normalization and fundamental removal, only the last 65,536 points were used in wavelet packet decomposition since the number of data points must be divisible by 2^{11}, where 11 is the number of WP decomposition levels. Each WP node would be equal to a 7.5 Hz band and contain $65{,}536/2^{11} = 32$ points which were used to compute the WP node's rms value.

The WP nodes of interest are ones that the characteristic frequencies fall into. The rms values of these WP nodes are used in clustering and in the proposed method.

At the fundamental of 15 Hz, the mechanical vibration of a bearing cage defect and a bearing outer race defect resulted in characteristic frequency at 5.98 and 47.87 Hz, respectively. Figure 4.10 and Figure 4.11 display the average WP node rms values of the current at the frequencies of interest for healthy, cage defect, and outer race defect bearings.

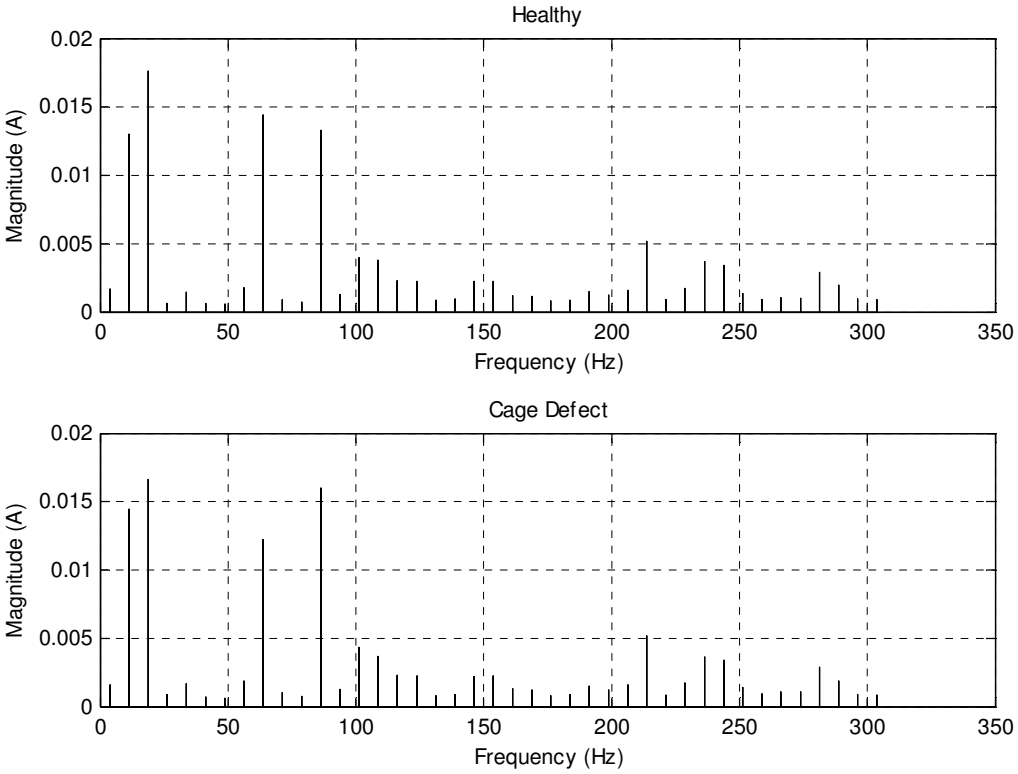

Figure 4.10. Average WP node rms values of the cage defect characteristic frequencies at the fundamental of 15 Hz

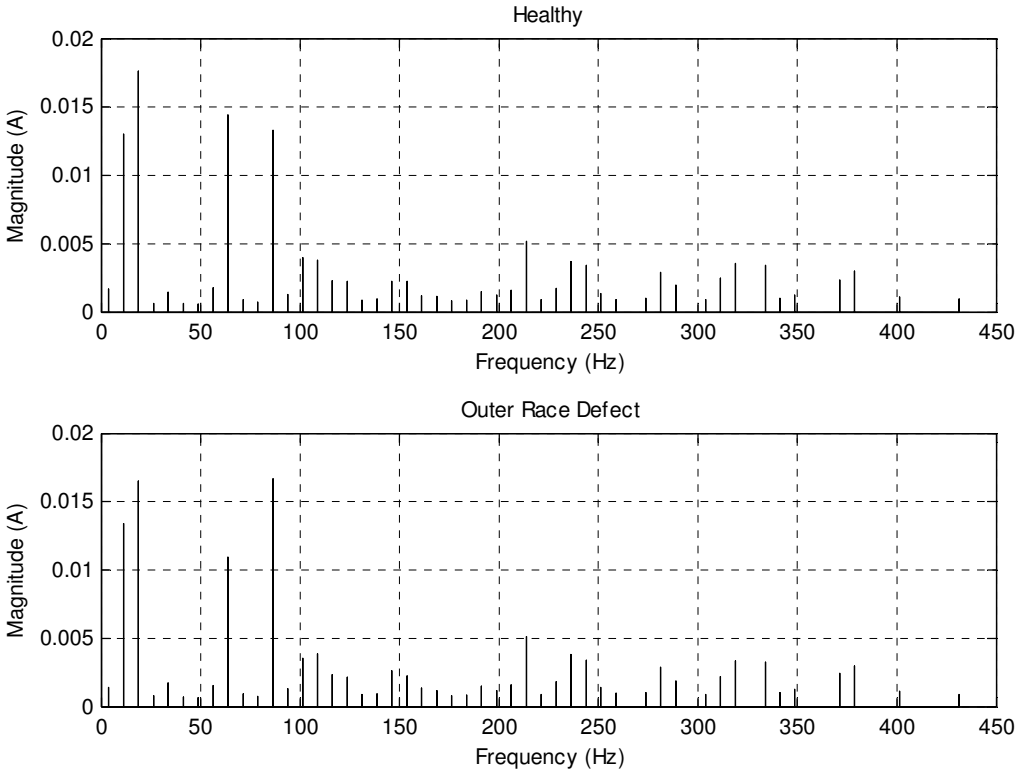

Figure 4.11. Average WP node rms values of the outer race defect characteristic frequencies at the fundamental of 15 Hz

At the fundamental of 30 Hz, the mechanical vibration of bearing cage defect and bearing outer race defect resulted in characteristic frequency at 11.98 and 95.84 Hz, respectively. Figure 4.12 and Figure 4.13 display the average WP node rms values of the current at the frequencies of interest for healthy, cage defect, and outer race defect bearings.

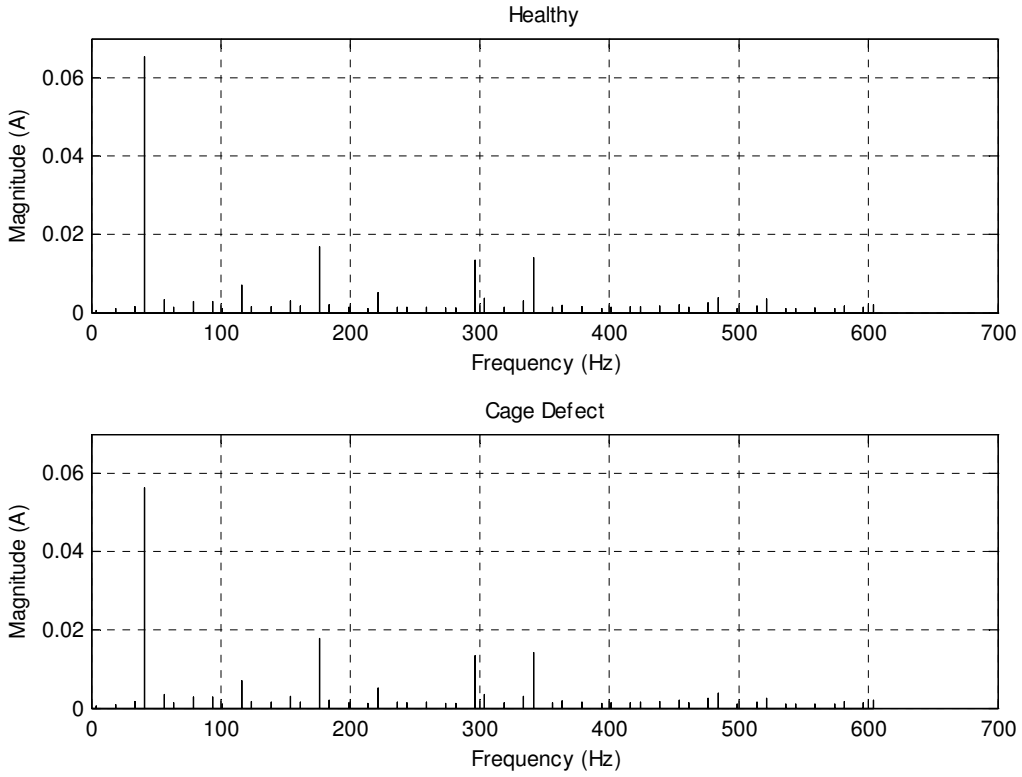

Figure 4.12. Average WP node rms values of the cage defect characteristic frequencies at the fundamental of 30 Hz

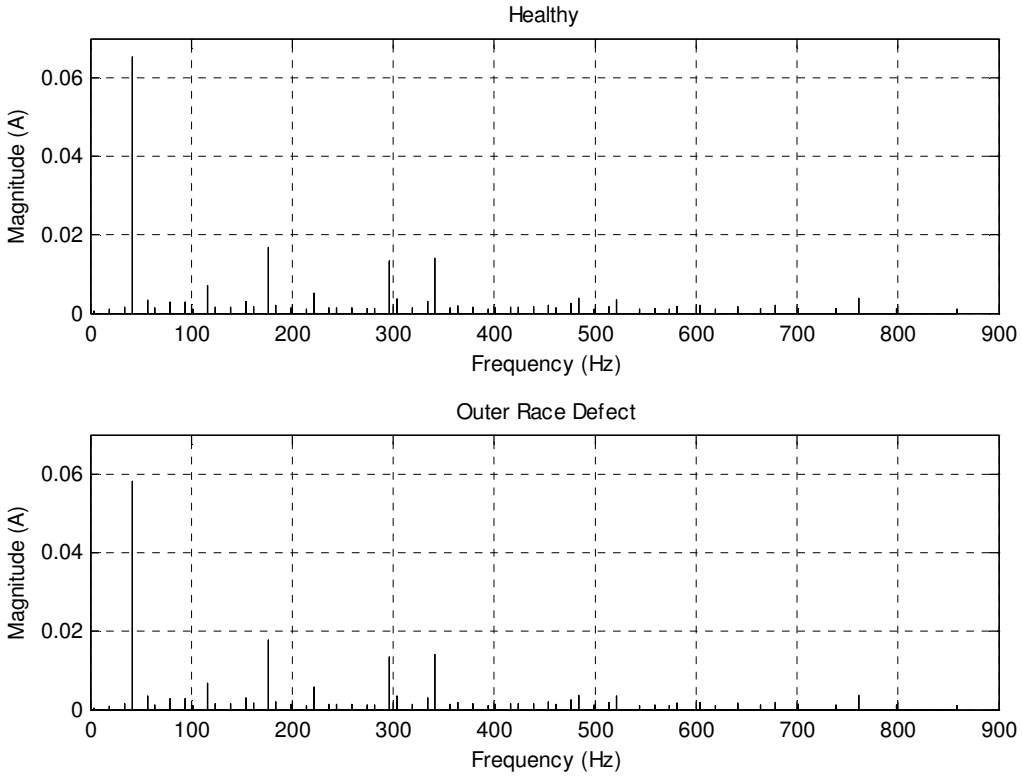

Figure 4.13. Average WP node rms values of the outer race defect characteristic frequencies at the fundamental of 30 Hz

At the fundamental of 45 Hz, the mechanical vibration of bearing cage defect and bearing outer race defect resulted in characteristic frequency at 17.98 and 143.84 Hz, respectively. Figure 4.14 and Figure 4.15 display the average WP node rms values of the current at the frequencies of interest for healthy, cage defect, and outer race defect bearings.

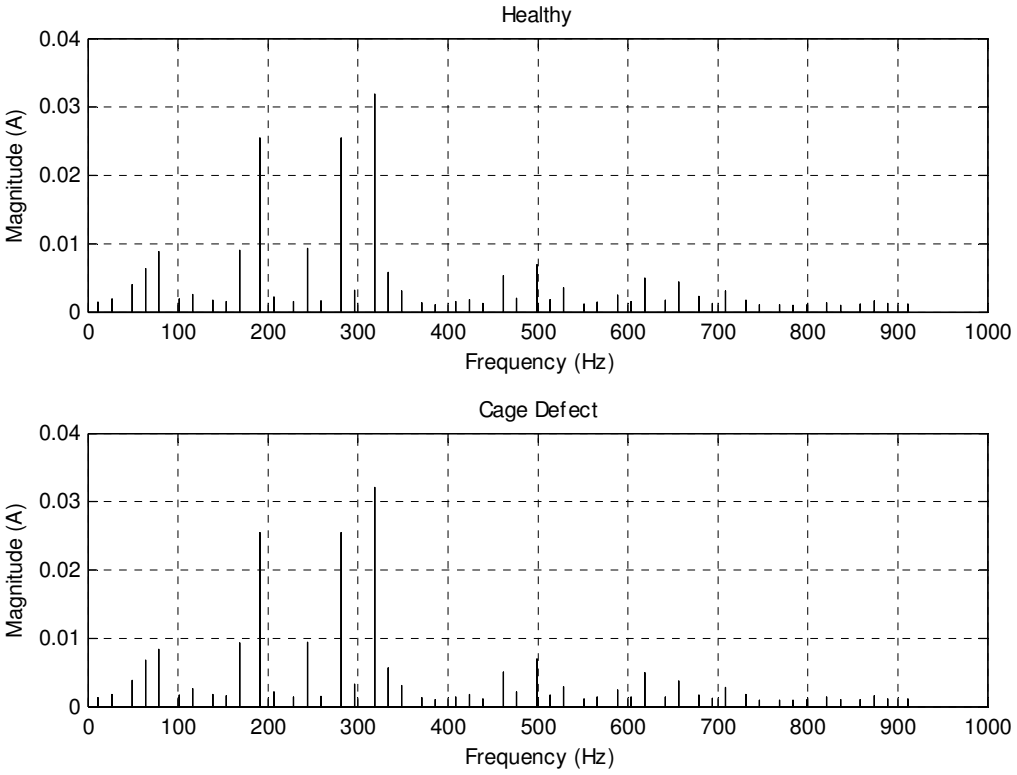

Figure 4.14. Average WP node rms values of the cage defect characteristic frequencies at the fundamental of 45 Hz

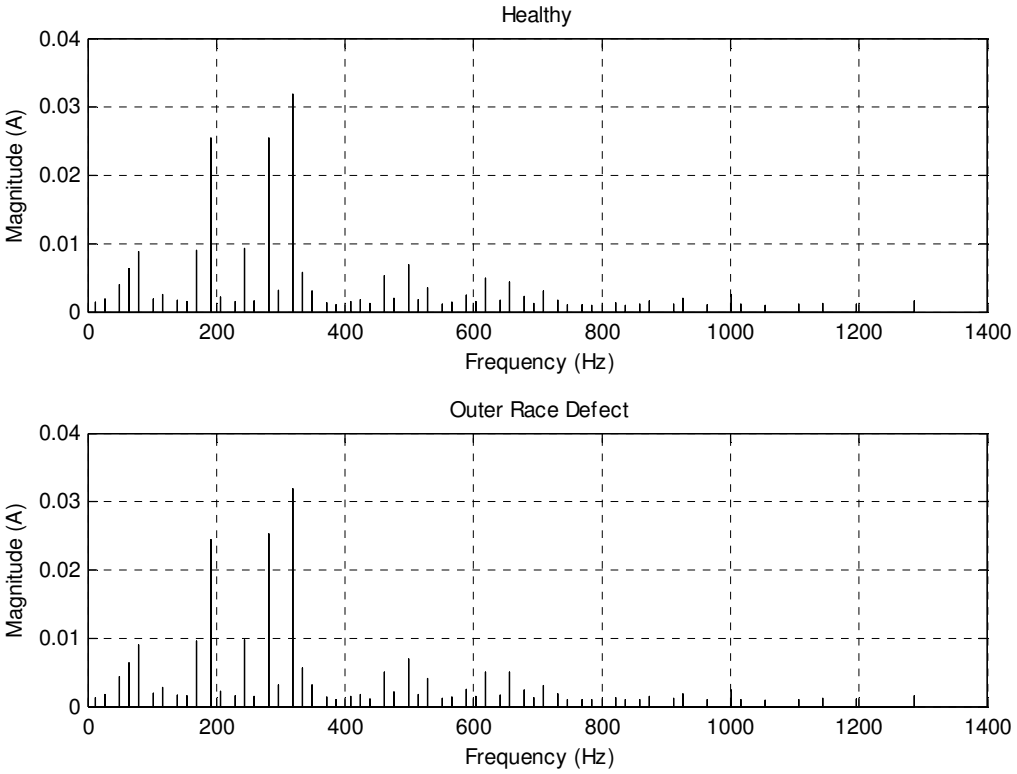

Figure 4.15. Average WP node rms values of the outer race defect characteristic frequencies at the fundamental of 45 Hz

At the fundamental of 60 Hz, the mechanical vibration of bearing cage defect and bearing outer race defect resulted in characteristic frequency at 23.97 and 191.79 Hz, respectively. Figure 4.16 and Figure 4.17 display the average WP node rms values of the current at the frequencies of interest for healthy, cage defect, and outer race defect bearings.

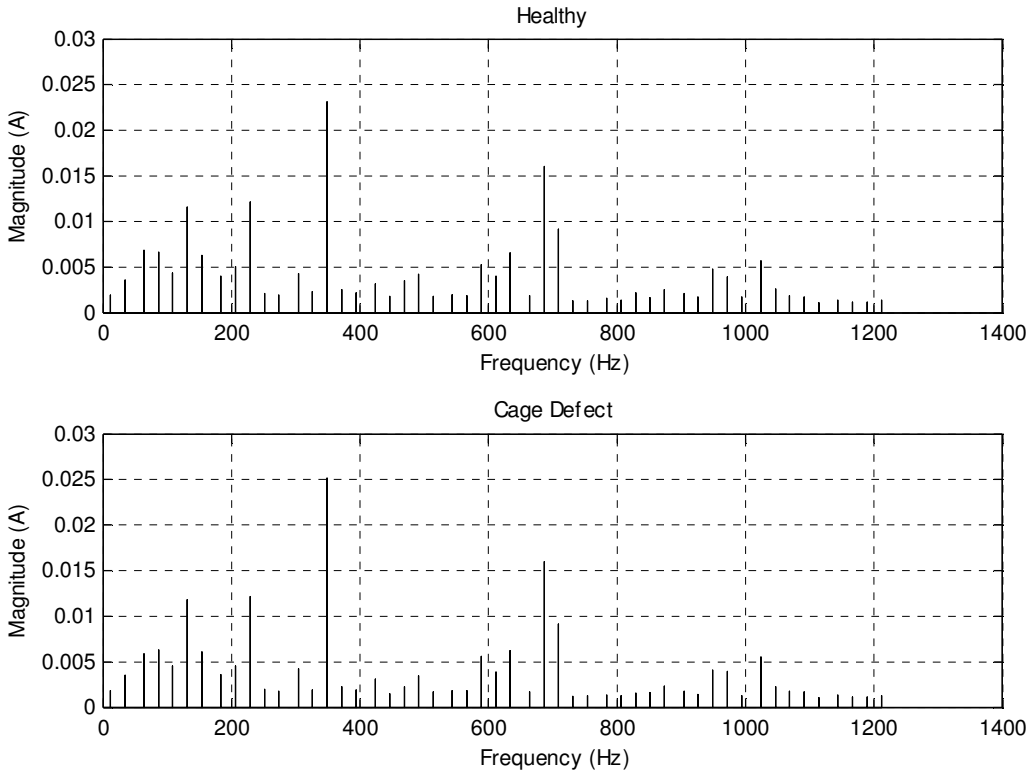

Figure 4.16. Average WP node rms values of the cage defect characteristic frequencies at the fundamental of 60 Hz

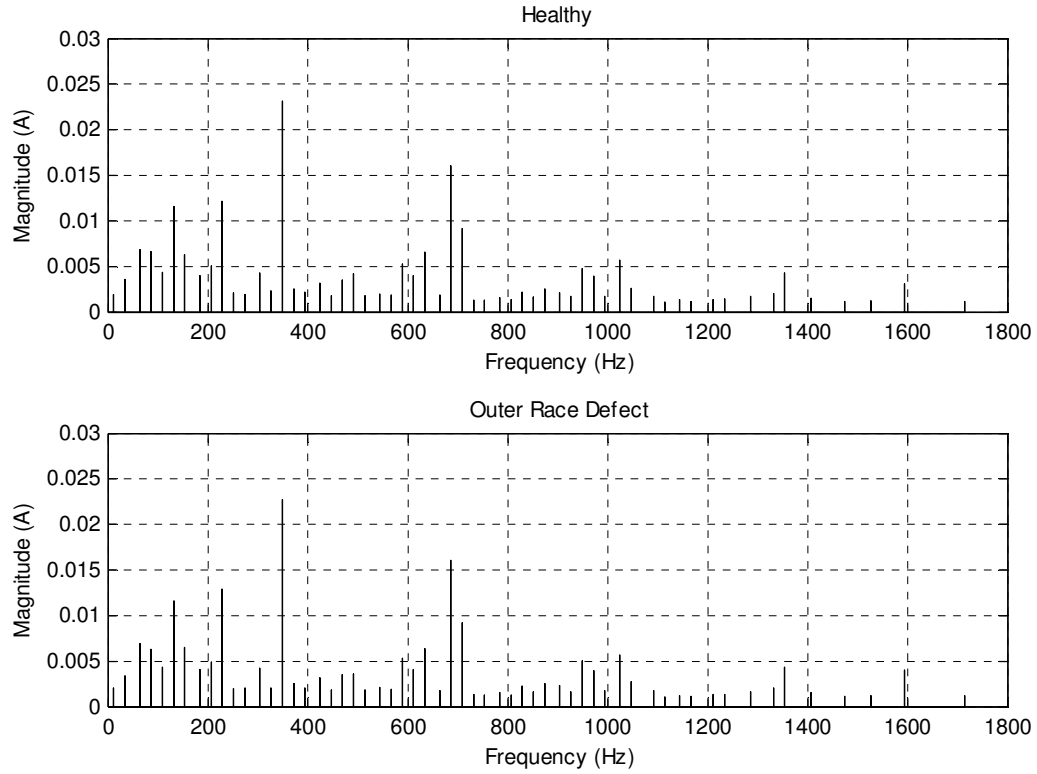

Figure 4.17. Average WP node rms values of the outer race defect characteristic frequencies at the fundamental of 60 Hz

The plots of the average WP rms values suggest that it is almost impossible to separate the healthy and defective bearings by simply comparing the WP rms values of the nodes of interest. The comparison of the results of clustering and the proposed method is shown below.

4.1 Results from Clustering

In the bearing cage defect case, the clustering classification error is shown in Figure 4.18. The plot reveals that the classification errors at the fundamentals of 15, 30, 45, and 60 Hz are 40%, 50%, 34%, and 43%, respectively.

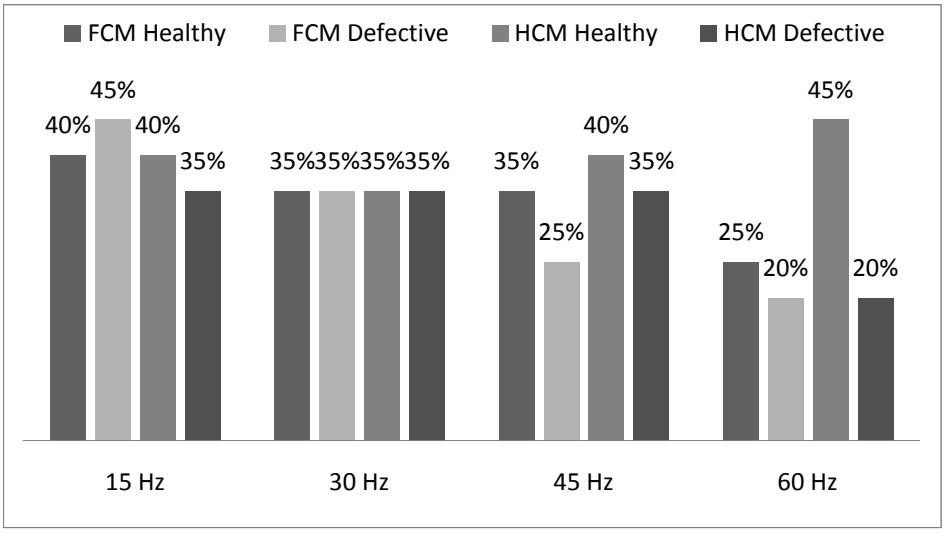

Figure 4.18. Clustering classification error for bearing cage defect

In the bearing outer race defect case, the clustering classification error is displayed in Figure 4.19. The plot shows that the classification errors at the fundamentals of 15, 30, 45, and 60 Hz are 38%, 47%, 28%, and 49%, respectively.

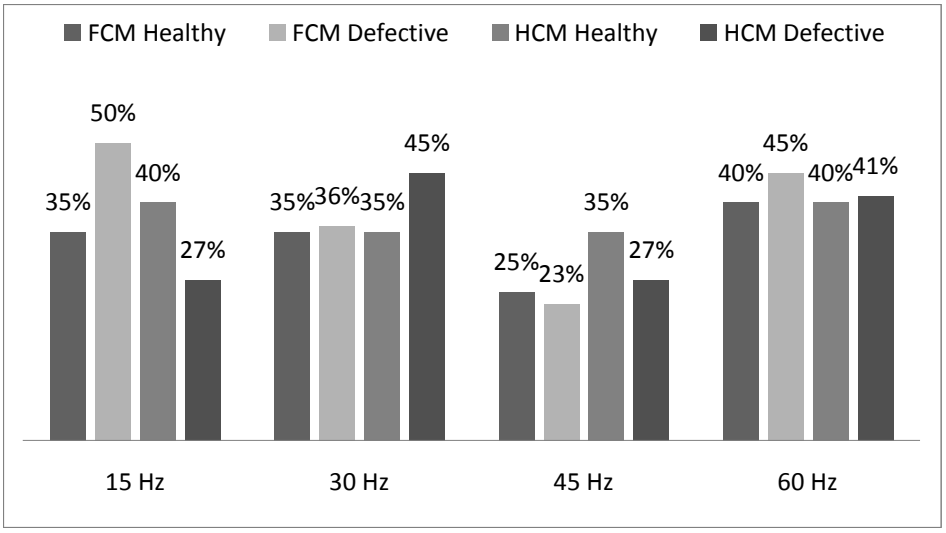

Figure 4.19. Clustering classification error for bearing outer race defect

In both bearing defect cases, these are close to random assignments. The results from clustering suggested that this method cannot find the similarity of the WP node rms values from healthy and defective bearings.

4.2 Results from the Proposed Method

In this section, the results of the proposed method are presented. The WP nodes of interest for each fundamental frequency and defect type were selected using the GA. The SVM determines the SVM classifier from the selected nodes. The SVM classifiers are then used to compute the 10-fold classification error. Three types of kernel functions, polynomials, radial basis function, hyperbolic tangent, were evaluated.

4.2.1 Cage Defect

In the cage defect case, the plot of the classification errors is depicted in Figure 4.20. The average percent errors categorized by the fundamental frequency are 5.62%, 11.7%, 16.9%, and 114.2% for 15, 30, 45, and 60 Hz, respectively. The average percent errors categorized by kernel functions are 11.7%, 14.4%, and 10.2% for polynomials, radial basis function, and hyperbolic tangent kernels, respectively.

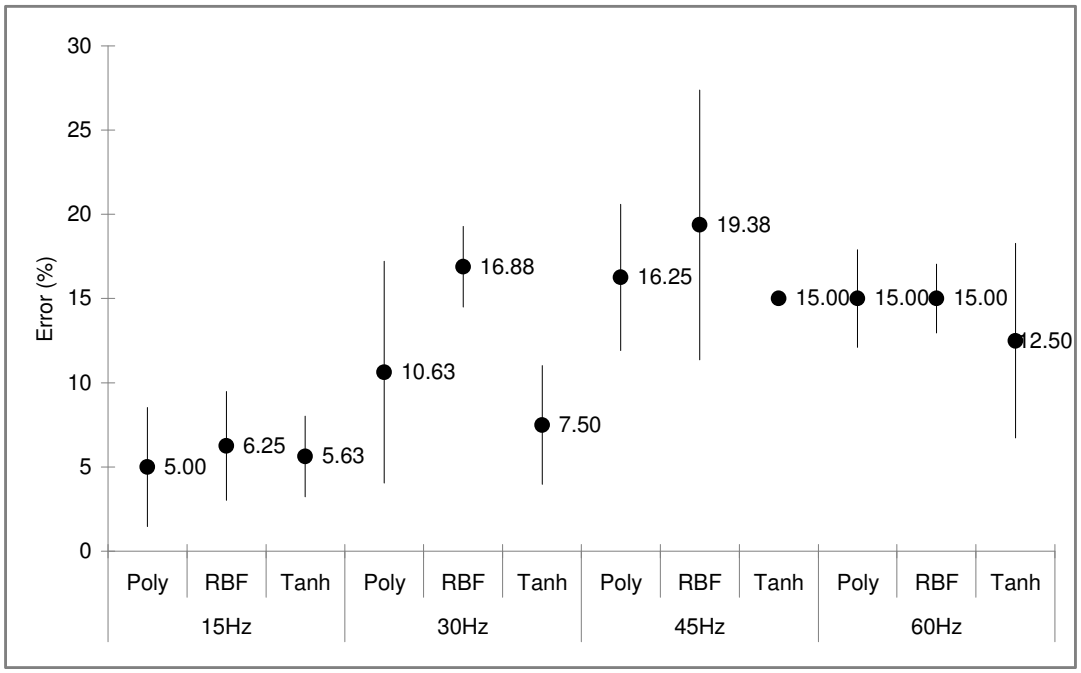

(a)

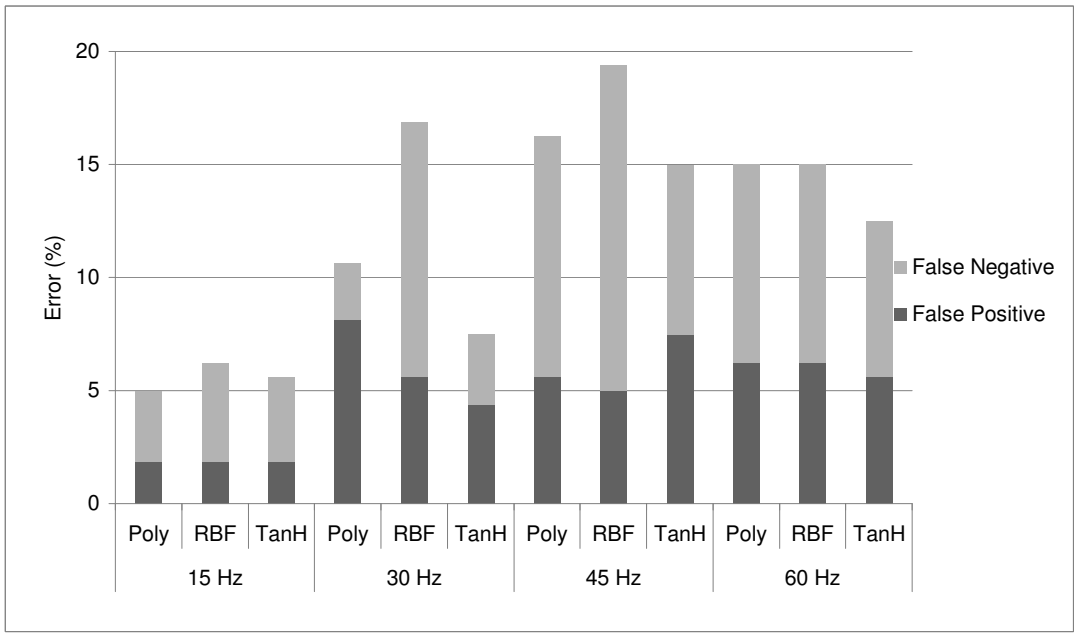

(b)

Figure 4.20. Average classification errors of the proposed method for bearing cage defect with (a) the standard deviation and (b) the average percent errors of false positive and false negative

The nodes selected by the GA and their corresponding frequency bands for the cage defect at the fundamental of 15, 30, 45, and 60 Hz are shown in Tables 4.1-4.4.

Poly			RBF			Tanh		
Node	Frequency Band (Hz)		Node	Frequency Band (Hz)		Node	Frequency Band (Hz)	
	Lower	Upper		Lower	Upper		Lower	Upper
2	7.5	15.0	5	30.0	37.5	5	30.0	37.5
4	22.5	30.0	7	45.0	52.5	6	37.5	45.0
5	30.0	37.5	8	52.5	60.0	7	45.0	52.5
6	37.5	45.0	11	75.0	82.5	8	52.5	60.0
8	52.5	60.0	12	82.5	90.0	9	60.0	67.5
9	60.0	67.5	22	157.5	165.0	19	135.0	142.5
14	97.5	105.0	24	172.5	180.0	23	165.0	172.5
17	120.0	127.5	25	180.0	187.5	24	172.5	180.0
18	127.5	135.0	26	187.5	195.0	29	210.0	217.5
19	135.0	142.5	30	217.5	225.0	30	217.5	225.0
21	150.0	157.5	34	247.5	255.0	31	225.0	232.5
23	165.0	172.5	38	277.5	285.0	32	232.5	240.0
25	180.0	187.5	39	285.0	292.5	36	262.5	270.0
28	202.5	210.0	40	292.5	300.0	37	270.0	277.5
30	217.5	225.0	41	300.0	307.5			
32	232.5	240.0						
41	300.0	307.5						

Table 4.1. Nodes selected by the GA and corresponding frequency bands for cage defect with the fundamental of 15 Hz

Poly			RBF			Tanh		
Node	Frequency Band (Hz)		Node	Frequency Band (Hz)		Node	Frequency Band (Hz)	
	Lower	Upper		Lower	Upper		Lower	Upper
1	0.0	7.5	3	15.0	22.5	6	37.5	45.0
6	37.5	45.0	8	52.5	60.0	11	75.0	82.5
16	112.5	120.0	11	75.0	82.5	14	97.5	105.0
19	135.0	142.5	16	112.5	120.0	16	112.5	120.0
29	210.0	217.5	17	120.0	127.5	22	157.5	165.0
30	217.5	225.0	32	232.5	240.0	25	180.0	187.5
33	240.0	247.5	41	300.0	307.5	29	210.0	217.5
35	255.0	262.5	43	315.0	322.5	30	217.5	225.0
41	300.0	307.5	54	397.5	405.0	33	240.0	247.5
43	315.0	322.5	56	412.5	420.0	37	270.0	277.5
49	360.0	367.5	61	450.0	457.5	40	292.5	300.0
53	390.0	397.5	65	480.0	487.5	41	300.0	307.5
54	397.5	405.0	69	510.0	517.5	45	330.0	337.5
57	420.0	427.5	70	517.5	525.0	46	337.5	345.0
61	450.0	457.5	73	540.0	547.5	51	375.0	382.5
62	457.5	465.0	80	592.5	600.0	54	397.5	405.0
67	495.0	502.5	81	600.0	607.5	59	435.0	442.5
69	510.0	517.5				61	450.0	457.5
70	517.5	525.0				67	495.0	502.5
77	570.0	577.5				69	510.0	517.5
80	592.5	600.0				70	517.5	525.0
						73	540.0	547.5
						78	577.5	585.0

Table 4.2. Nodes selected by the GA and corresponding frequency bands for cage defect with the fundamental of 30 Hz

Poly			RBF			Tanh		
Node	Frequency Band (Hz)		Node	Frequency Band (Hz)		Node	Frequency Band (Hz)	
	Lower	Upper		Lower	Upper		Lower	Upper
7	45.0	52.5	14	97.5	105.0	7	45.0	52.5
11	75.0	82.5	19	135.0	142.5	9	60.0	67.5
14	97.5	105.0	21	150.0	157.5	16	112.5	120.0
16	112.5	120.0	35	255.0	262.5	28	202.5	210.0
19	135.0	142.5	38	277.5	285.0	33	240.0	247.5
21	150.0	157.5	50	367.5	375.0	35	255.0	262.5
43	315.0	322.5	55	405.0	412.5	40	292.5	300.0
45	330.0	337.5	64	472.5	480.0	43	315.0	322.5
52	382.5	390.0	81	600.0	607.5	71	525.0	532.5
59	435.0	442.5	86	637.5	645.0	79	585.0	592.5
64	472.5	480.0	95	705.0	712.5	86	637.5	645.0
67	495.0	502.5	105	780.0	787.5	88	652.5	660.0
71	525.0	532.5	112	832.5	840.0	91	675.0	682.5
74	547.5	555.0	115	855.0	862.5	95	705.0	712.5
86	637.5	645.0	117	870.0	877.5	105	780.0	787.5
88	652.5	660.0	122	907.5	915.0	107	795.0	802.5
98	727.5	735.0				115	855.0	862.5
105	780.0	787.5						
107	795.0	802.5						
110	817.5	825.0						
115	855.0	862.5						
117	870.0	877.5						
119	885.0	892.5						

Table 4.3. Nodes selected by the GA and corresponding frequency bands for cage defect with the fundamental of 45 Hz

Poly			RBF			Tanh		
Node	Frequency Band (Hz)		Node	Frequency Band (Hz)		Node	Frequency Band (Hz)	
	Lower	Upper		Lower	Upper		Lower	Upper
9	60.0	67.5	9	60.0	67.5	2	7.5	15.0
12	82.5	90.0	12	82.5	90.0	5	30.0	37.5
15	105.0	112.5	15	105.0	112.5	12	82.5	90.0
21	150.0	157.5	25	180.0	187.5	25	180.0	187.5
25	180.0	187.5	28	202.5	210.0	28	202.5	210.0
34	247.5	255.0	31	225.0	232.5	31	225.0	232.5
37	270.0	277.5	34	247.5	255.0	34	247.5	255.0
47	345.0	352.5	37	270.0	277.5	37	270.0	277.5
53	390.0	397.5	47	345.0	352.5	47	345.0	352.5
57	420.0	427.5	57	420.0	427.5	60	442.5	450.0
63	465.0	472.5	66	487.5	495.0	66	487.5	495.0
66	487.5	495.0	82	607.5	615.0	69	510.0	517.5
92	682.5	690.0	85	630.0	637.5	73	540.0	547.5
98	727.5	735.0	89	660.0	667.5	76	562.5	570.0
108	802.5	810.0	92	682.5	690.0	85	630.0	637.5
114	847.5	855.0	101	750.0	757.5	89	660.0	667.5
117	870.0	877.5	105	780.0	787.5	105	780.0	787.5
130	967.5	975.0	108	802.5	810.0	108	802.5	810.0
137	1020.0	1027.5	124	922.5	930.0	111	825.0	832.5
146	1087.5	1095.0	130	967.5	975.0	114	847.5	855.0
153	1140.0	1147.5	133	990.0	997.5	124	922.5	930.0
156	1162.5	1170.0	149	1110.0	1117.5	130	967.5	975.0
159	1185.0	1192.5	153	1140.0	1147.5	133	990.0	997.5
			156	1162.5	1170.0	140	1042.5	1050.0
			159	1185.0	1192.5	149	1110.0	1117.5

Table 4.4. Nodes selected by the GA and corresponding frequency bands for cage defect with the fundamental of 60 Hz

4.2.2 Outer Race Defect

In the outer race defect case, the plot of the classification errors is depicted in Figure 4.21. The average percent errors categorized by the fundamental frequency are 12.3%, 14.1%, 7.74%, and 20.0% for 15, 30, 45, and 60 Hz, respectively. The average percent errors categorized by kernel functions are 13.2%, 13.8%, and 13.5% for polynomials, radial basis function, and hyperbolic tangent kernels, respectively.

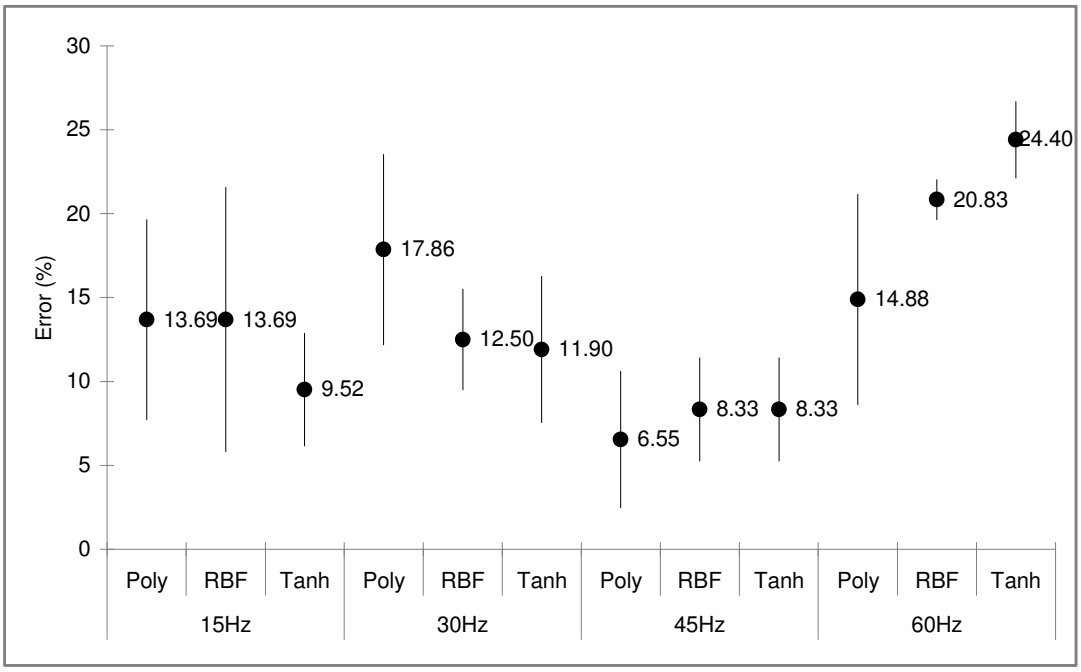

(a)

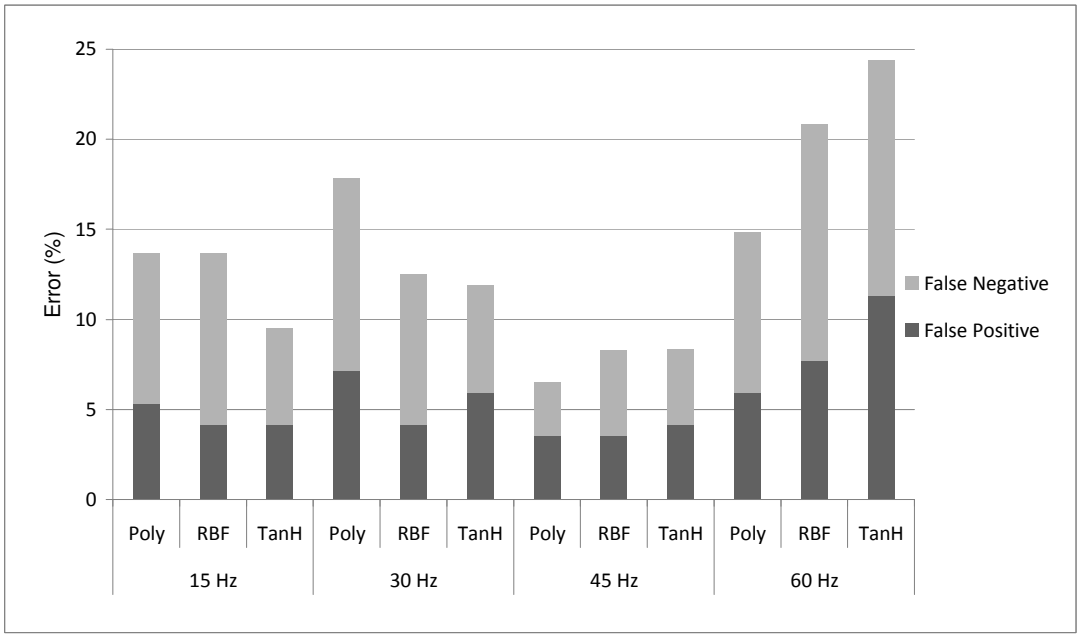

(b)

Figure 4.21. Average classification errors of the proposed method for bearing outer race defect with (a) the standard deviation and (b) the average percent errors of false positive and false negative

The nodes selected by the GA and their corresponding frequency bands for the outer race defect at the fundamental of 15, 30, 45, and 60 Hz are shown in Tables 4.1-4.4.

Poly			RBF			Tanh		
Node	Frequency Band (Hz)		Node	Frequency Band (Hz)		Node	Frequency Band (Hz)	
	Lower	Upper		Lower	Upper		Lower	Upper
1	0.0	7.5	1	0.0	7.5	1	0.0	7.5
3	15.0	22.5	4	22.5	30.0	2	7.5	15.0
6	37.5	45.0	14	97.5	105.0	5	30.0	37.5
9	60.0	67.5	15	105.0	112.5	6	37.5	45.0
10	67.5	75.0	16	112.5	120.0	9	60.0	67.5
13	90.0	97.5	17	120.0	127.5	11	75.0	82.5
14	97.5	105.0	20	142.5	150.0	14	97.5	105.0
15	105.0	112.5	25	180.0	187.5	15	105.0	112.5
16	112.5	120.0	31	225.0	232.5	16	112.5	120.0
19	135.0	142.5	32	232.5	240.0	18	127.5	135.0
20	142.5	150.0	33	240.0	247.5	19	135.0	142.5
22	157.5	165.0	34	247.5	255.0	20	142.5	150.0
25	180.0	187.5	41	300.0	307.5	26	187.5	195.0
29	210.0	217.5	42	307.5	315.0	29	210.0	217.5
30	217.5	225.0	43	315.0	322.5	31	225.0	232.5
32	232.5	240.0	47	345.0	352.5	32	232.5	240.0
33	240.0	247.5	58	427.5	435.0	33	240.0	247.5
42	307.5	315.0				35	255.0	262.5
43	315.0	322.5				38	277.5	285.0
45	330.0	337.5				39	285.0	292.5
46	337.5	345.0				42	307.5	315.0
58	427.5	435.0				43	315.0	322.5
						45	330.0	337.5
						54	397.5	405.0

Table 4.5. Nodes selected by the GA and corresponding frequency bands for outer race defect with the fundamental of 15 Hz

Poly			RBF			Tanh		
Node	Frequency Band (Hz)		Node	Frequency Band (Hz)		Node	Frequency Band (Hz)	
	Lower	Upper		Lower	Upper		Lower	Upper
8	52.5	60.0	5	30.0	37.5	6	37.5	45.0
9	60.0	67.5	6	37.5	45.0	8	52.5	60.0
11	75.0	82.5	8	52.5	60.0	9	60.0	67.5
13	90.0	97.5	16	112.5	120.0	19	135.0	142.5
22	157.5	165.0	17	120.0	127.5	24	172.5	180.0
24	172.5	180.0	22	157.5	165.0	32	232.5	240.0
25	180.0	187.5	24	172.5	180.0	37	270.0	277.5
33	240.0	247.5	25	180.0	187.5	40	292.5	300.0
43	315.0	322.5	29	210.0	217.5	43	315.0	322.5
45	330.0	337.5	37	270.0	277.5	45	330.0	337.5
53	390.0	397.5	38	277.5	285.0	53	390.0	397.5
61	450.0	457.5	40	292.5	300.0	56	412.5	420.0
62	457.5	465.0	46	337.5	345.0	61	450.0	457.5
65	480.0	487.5	48	352.5	360.0	62	457.5	465.0
67	495.0	502.5	49	360.0	367.5	65	480.0	487.5
77	570.0	577.5	51	375.0	382.5	67	495.0	502.5
78	577.5	585.0	53	390.0	397.5	69	510.0	517.5
81	600.0	607.5	62	457.5	465.0	73	540.0	547.5
89	660.0	667.5	65	480.0	487.5	81	600.0	607.5
91	675.0	682.5	67	495.0	502.5	89	660.0	667.5
99	735.0	742.5	77	570.0	577.5	91	675.0	682.5
102	757.5	765.0	91	675.0	682.5	94	697.5	705.0
			102	757.5	765.0	102	757.5	765.0

Table 4.6. Nodes selected by the GA and corresponding frequency bands for outer race defect with the fundamental of 30 Hz

Poly			RBF			Tanh		
Node	Frequency Band (Hz)		Node	Frequency Band (Hz)		Node	Frequency Band (Hz)	
	Lower	Upper		Lower	Upper		Lower	Upper
2	7.5	15.0	2	7.5	15.0	2	7.5	15.0
11	75.0	82.5	16	112.5	120.0	7	45.0	52.5
16	112.5	120.0	19	135.0	142.5	11	75.0	82.5
19	135.0	142.5	23	165.0	172.5	16	112.5	120.0
26	187.5	195.0	26	187.5	195.0	21	150.0	157.5
28	202.5	210.0	28	202.5	210.0	23	165.0	172.5
33	240.0	247.5	35	255.0	262.5	33	240.0	247.5
35	255.0	262.5	38	277.5	285.0	35	255.0	262.5
38	277.5	285.0	43	315.0	322.5	38	277.5	285.0
43	315.0	322.5	50	367.5	375.0	43	315.0	322.5
47	345.0	352.5	52	382.5	390.0	45	330.0	337.5
52	382.5	390.0	55	405.0	412.5	55	405.0	412.5
62	457.5	465.0	59	435.0	442.5	59	435.0	442.5
64	472.5	480.0	62	457.5	465.0	62	457.5	465.0
69	510.0	517.5	67	495.0	502.5	69	510.0	517.5
71	525.0	532.5	71	525.0	532.5	74	547.5	555.0
86	637.5	645.0	76	562.5	570.0	76	562.5	570.0
100	742.5	750.0	81	600.0	607.5	81	600.0	607.5
103	765.0	772.5	86	637.5	645.0	83	615.0	622.5
110	817.5	825.0	91	675.0	682.5	86	637.5	645.0
112	832.5	840.0	93	690.0	697.5	88	652.5	660.0
124	922.5	930.0	98	727.5	735.0	93	690.0	697.5
129	960.0	967.5	103	765.0	772.5	95	705.0	712.5
134	997.5	1005.0	110	817.5	825.0	100	742.5	750.0
141	1050.0	1057.5	117	870.0	877.5	103	765.0	772.5
148	1102.5	1110.0	134	997.5	1005.0	105	780.0	787.5
172	1282.5	1290.0	136	1012.5	1020.0	110	817.5	825.0
			141	1050.0	1057.5	112	832.5	840.0
			148	1102.5	1110.0	115	855.0	862.5
			160	1192.5	1200.0	117	870.0	877.5
						124	922.5	930.0
						129	960.0	967.5
						134	997.5	1005.0
						136	1012.5	1020.0
						141	1050.0	1057.5
						160	1192.5	1200.0

Table 4.7. Nodes selected by the GA and corresponding frequency bands for outer race defect with the fundamental of 45 Hz

Poly			RBF			Tanh		
Node	Frequency Band (Hz)		Node	Frequency Band (Hz)		Node	Frequency Band (Hz)	
	Lower	Upper		Lower	Upper		Lower	Upper
2	7.5	15.0	2	7.5	15.0	2	7.5	15.0
21	150.0	157.5	5	30.0	37.5	5	30.0	37.5
25	180.0	187.5	12	82.5	90.0	18	127.5	135.0
31	225.0	232.5	21	150.0	157.5	21	150.0	157.5
44	322.5	330.0	34	247.5	255.0	34	247.5	255.0
66	487.5	495.0	41	300.0	307.5	41	300.0	307.5
85	630.0	637.5	44	322.5	330.0	44	322.5	330.0
89	660.0	667.5	57	420.0	427.5	57	420.0	427.5
95	705.0	712.5	66	487.5	495.0	66	487.5	495.0
105	780.0	787.5	69	510.0	517.5	69	510.0	517.5
124	922.5	930.0	76	562.5	570.0	76	562.5	570.0
127	945.0	952.5	85	630.0	637.5	79	585.0	592.5
133	990.0	997.5	108	802.5	810.0	101	750.0	757.5
137	1020.0	1027.5	133	990.0	997.5	108	802.5	810.0
149	1110.0	1117.5	146	1087.5	1095.0	114	847.5	855.0
153	1140.0	1147.5	156	1162.5	1170.0	117	870.0	877.5
162	1207.5	1215.0	162	1207.5	1215.0	121	900.0	907.5
181	1350.0	1357.5	178	1327.5	1335.0	124	922.5	930.0
213	1590.0	1597.5	181	1350.0	1357.5	127	945.0	952.5
			188	1402.5	1410.0	133	990.0	997.5
						137	1020.0	1027.5
						140	1042.5	1050.0
						165	1230.0	1237.5
						172	1282.5	1290.0
						178	1327.5	1335.0
						181	1350.0	1357.5
						188	1402.5	1410.0
						204	1522.5	1530.0
						213	1590.0	1597.5

Table 4.8. Nodes selected by the GA and corresponding frequency bands for outer race defect with the fundamental of 60 Hz

In this chapter, the results from the clustering and the proposed method were presented. The clustering method has been shown that it is not to be unsuitable for this problem due to high classification errors. The proposed method has been shown to be able to classify healthy and defective bearings from the captured current waveforms.

CHAPTER 5 CONCLUSION

Bearing faults are a major problem found in adjustable speed drives. Though bearings are inexpensive to replace, their problems are the most difficult to detect and their failures can cause significant losses. In this dissertation, bearing fault detection in an ASD system was performed from the drive current waveforms. As a variation of the original MCSA, the method utilized various techniques, including wavelet packet decomposition, the support vector machine, and the genetic algorithm. The application of the proposed method is shown to provide a useful diagnosis for ASD bearing fault detection.

5.1 Summary

The background information on adjustable speed drives and ball bearings as well as the detail theory of the techniques was provided in Chapter 2. The proposed method, described in Chapter 3, is an integration of signal processing, including wavelet packet decomposition, the support vector machine, and the genetic algorithm. The machine current data is decomposed into wavelet packet nodes. Since the ASD current contained high level of EMI noise, which lowers the significance of the characteristic bearing fault frequency components, the GA is applied to help determine the wavelet packet nodes that should be chosen as features to create an SVM classifier. Chapter 4 showed that the proposed method produces reasonable classification results.

Since ASD systems are not identical, their characteristic may vary from one to another and the EMI noise and other interference conditions may also vary and, as a

result, the proposed method must be carried-out on each individual drive in order to accurately detect bearing faults in different systems.

To implement bearing fault detection using the proposed method in the currently available commercial circuit monitors, the SVM classifier for each bearing fault type needs to be pre-determined. Since the WP nodes affected by the faults are known, wavelet packet decomposition with pruning can be used. With pruning, only the branches leading to the nodes are computed. This should reduce the computational complexity in the circuit monitor considerably. Then, the WP node rms values are computed and the SVM classifier can be applied to the rms values to determine the bearing condition.

5.2 Future Work

This dissertation showed that wavelet packet decomposition and the support vector machine with feature selection using the genetic algorithm provides a good method for bearing fault detection in adjustable speed drives. Two different bearing fault conditions, cage defects and outer race defects, were evaluated. Future work should possibly be focused on:

1. The study of other bearing fault types, inner race defects and ball defects, and other motor faults, such as broken rotor bars.
2. The generalization of SVM classifiers for each motor drive model.

The proposed method has shown promises for other bearing fault types and other kinds of motor faults. Since, like other rotating machines, most faults in ASD's are periodic and the current signal also suffers from the PWM switching and EMI noise, the

same method would help determine the frequency components that most affect the system. The SVM classifiers can then be obtained.

The proposed method is now not completely commercially feasible due to the fact that the resulting SVM classifiers may be different from one individual machine to another. In this dissertation, only one ASD drive was available for the experiment. The characteristics of each motor drive could be different, which results in different selected WP nodes and, thus, different SVM classifiers. SVM classifiers must be determined for each ASD motor combination. This is not very effective for the method to be commercially deployed. It is more desirable to have SVM classifiers that can classify all ASD motors of the same model. For this, further study is required.

BIBLIOGRAPHY

[1] R. R. Schoen, T. G. Habetler, F. Kamran, and R. G. Bartheld, "Motor Bearing Damage Detection Using Stator Current Monitoring," IEEE Trans. Ind. Applicat., vol. 31, pp. 1274-9, Nov./Dec. 1995.

[2] J. Anderson, S. Lebruska, Stress Related Failures and Testing of Inverter Driven Motors, Baker Instrument Company.

[3] D. Busse, J. Erdman, R. Kerkman, D. Schlegel, and G. Skibinski, "Characteristics of shaft voltage and bearing currents," IEEE Industry Applications Magazine, vol. 3, Issue 6, pp. 21 – 32. Nov.-Dec. 1997.

[4] S. Bell, T. j. Cookson, S. A. Cope, R. A. Epperly, et. al., "Experience With Variable-Frequency Drives and Motor Bearing Reliability," IEEE Trans. Industry Applications, vol. 37, no. 5, pp. 1438-46, Sep./Oct.2001.

[5] B. Akin, H. A. Toliyat, U. Orguner, and M. Rayner, "PWM Inverter Harmonics Contributions to the Inverter-Fed Induction Machine Bearing Fault Diagnosis," IEEE Applied Power Electronics Conf., pp. 1393-1399, Feb.-Mar. 2007.

[6] L. Eren, "Bearing Damage Detection via Wavelet Packet Decomposition of Stator Current," Ph.D. dissertation, University of Missouri, Columbia, Dec. 2002.

[7] L. Eren and M. J. Devaney, "Motor Current Analysis via Wavelet Transform with Spectral Post-Processing for Bearing Fault Detection," IEEE Instrumentation and Measurement Technology Conference, pp. 411-4, May 2003.

[8] L. Eren, M. Ünal, and M. J. Devaney, "Harmonic Analysis via Wavelet Packet Decomposition using Special Elliptic Half-Band Filters," IEEE Instrumentation and Measurement Technology Conference, pp. 2111-4, May 2004.

[9] L. Eren and M. J. Devaney, "Bearing Damage Detection via Wavelet Packet Decomposition of the Stator Current," IEEE Trans. Instrum. Meas., vol. 53, pp. 431-6, Apr. 2004.

[10] W. Yoon and M. J. Devaney, "Power Measurement Using the Wavelet Transform," IEEE Trans. Instrum. Meas., vol. 47, no. 5, pp. 1205-10, Oct. 1998.

[11] R. C. Kryter and H. D. Haynes, "Condition monitoring of machinery using motor current signature analysis," Sound and Vibration, pp. 14-21, Sept. 1989.

[12] G.B. Kliman, W.J. Premerlani, B. Yazici, R.A. Koegl, and J. Mazereeuw, "Sensorless online motor diagnostics," IEEE Comput. Appl. Power, vol. 10, no. 2, pp. 39–43, 1997.

[13] Y. Zhongming, B. Wu, and A. R. Sadeghian, "Signature analysis of induction motor mechanical faults by wavelet packet decomposition," Sixteenth Annual IEEE Applied Power Electronics Conference and Exposition, vol. 2, pp. 1022-29, 2001.

[14] A. H. Bonnett, "Analysis of the Impact of Pulse-Width Modulated Inverter Voltage Waveforms on AC Induction Motors." IEEE Trans. Ind. Applicat., vol. 32, pp. 386-392, Mar./Apr. 1996.

[15] W. Shepherd, L. N. Hulley, and D. T. W. Liang, Power Electronics and Motor Control, New York: Cambridge University Press, 1996.

[16] H. Kiesel and M. Holland, "No bearing problems," IEEE/PCA Cement Industry Technical Conference Proceedings, pp. 19-28, May 2000.

[17] B. K. N. Rao, Handbook of Condition Monitoring, Elsevier Advanced Technology, Oxford, UK, 1996.

[18] C. M. Riley, B. K. Lin, T. G. Habetler, and R. R. Schoen, "A method for sensorless on-line vibration monitoring of induction machines," IEEE Trans. Industry Applications, Vol. 34, no. 6, pp. 1240-5, Nov/Dec 1998.

[19] C. M. Riley, B. K. Lin, T. G. Habetler, and G. B. Kliman, "Stator current harmonics and their causal vibrations: a preliminary investigation of sensorless vibration monitoring applications," IEEE Trans. Industry Applications, Vol. 35, no. 1, pp. 94-9, Jan/Feb 1999.

[20] Application Note 243-1, "Effective Machinery Measurements using Dynamic Signal Analyzers," Hewlett Packard.

[21] S. Mallat, A Wavelet Tour of Signal Processing, 2nd Edition, Academic Press, London, 1999.

[22] A. P. Engelbrecht, Computational Intelligence: An Introduction, West Sussex, England: Wiley, 2002.

[23] B. K. Bose , Power Electronics and AC Drives, New Jersey: Prentice-Hall, 1986.

[24] P. J. Link, "Minimizing electric bearing currents in adjustable speed drive systems," Pulp and Paper Industry Technical Conference 1998, Conference Record of 1998 Annual 21-26, pp. 181 – 195, Jun. 1998.

[25] A. Jensen and A. la Cour-Harbo, Ripples in Mathematics The Discrete Wavelet Transorm, Springer, New York, 2001.

[26] D. F. Mix and K. J. Olejniczak, Elements of Wavelets for Engineers and Scientists, New Jersey: Wiley, 2003.

[27] A. K. Chan, Wavelets for Sensing Technologies, Boston: Artech House Publishers, 2003.

[28] S. Jaffard, Y. Meyer, and R. D. Ryan, Wavelets: Tools for Science & Technology, Philadelphia: Soc for Industrial & Applied Math, 2001.

[29] C. Blatter, Wavelets: A Primer, Natick, MA: A K Peters, 1998.

[30] N. Chen, W. Lu, J. Yang, and G. Li, Support Vector Machine in Chemistry, World Scientific, New Jersey, 2004.

[31] S. Theodoridis and K. Koutroumbas, Pattern Recognition, 2nd Edition, Academic Press, New York, 2003.

VITA

Lt. Kaptan Teotrakool was born on September 21, 1974 in Bangkok, Thailand. He attended elementary and junior high schools in Bangkok. In 1991, he was accepted into the Armed Forces Academies Preparatory School. In 1993, he entered the Royal Thai Naval Academy. He was awarded a scholarship from the Royal Thai Naval Academy to pursue a bachelor's degree in Electrical and Computer Engineering at the University of Missouri-Columbia in 1994. He earned Bachelors of Science in Electrical Engineering and Computer Engineering in 1998 and further continued a Master of Science study in Electrical Engineering. After having earned his master's degree in 2000, Lt. Teotrakool returned to Thailand where he worked for the Royal Thai Navy as an electronics chief engineer and network engineer. He also lectured at several universities in Thailand. In 2003, Lt. Teotrakool continued his Doctor of Philosophy study in Electrical and Computer Engineering at the University of Missouri-Columbia. During his years as a graduate student, Lt. Teotrakool worked as a graduate teaching assistant, graduate research assistant, and graduate instructor for the Departments of Electrical and Computer Engineering.

Lt. Teotrakool married Arunee Raksasatya Teotrakool on April 20th, 2002. Currently, the couple and their son Akira Keene Teotrakool plan to return to Thailand after his graduation.